
GRAPH ALIGNMENT VIA DUAL-PASS SPECTRAL ENCODING AND LATENT SPACE COMMUNICATION

Maysam Behmanesh, Erkan Turan & Maks Ovsjanikov
LIX, École Polytechnique, IP Paris

ABSTRACT

Graph alignment, the problem of identifying corresponding nodes across multiple graphs, is fundamental to numerous applications. Most existing unsupervised methods embed node features into latent representations to enable cross-graph comparison without ground-truth correspondences. However, these methods suffer from two critical limitations: the degradation of node distinctiveness due to oversmoothing in GNN-based embeddings, and the misalignment of latent spaces across graphs caused by structural noise, feature heterogeneity, and training instability, ultimately leading to unreliable node correspondences. We propose a novel graph alignment framework that simultaneously enhances node distinctiveness and enforces geometric consistency across latent spaces. Our approach introduces a dual-pass encoder that combines low-pass and high-pass spectral filters to generate embeddings that are both structure-aware and highly discriminative. To address latent space misalignment, we incorporate a geometry-aware functional map module that learns bijective and isometric transformations between graph embeddings, ensuring consistent geometric relationships across different representations. Extensive experiments on graph benchmarks demonstrate that our method consistently outperforms existing unsupervised alignment baselines, exhibiting superior robustness to structural inconsistencies and challenging alignment scenarios. Additionally, comprehensive evaluation on vision-language benchmarks using diverse pretrained models shows that our framework effectively generalizes beyond graph domains, enabling unsupervised alignment of vision and language representations.

1 INTRODUCTION

Graph alignment, also referred to as network alignment or graph matching, is a fundamental problem in machine learning and graph theory, concerned with identifying a correspondence between the nodes of two graphs such that structurally similar or semantically equivalent nodes are matched.

Graph alignment arises in a wide range of application domains, including bioinformatics (e.g., protein interaction networks) (Liao et al., 2009; Singh et al., 2007), social network analysis (Li et al., 2018; Korula & Lattanzi, 2014), computer vision (Liu et al., 2022a; Chen et al., 2025; Wang et al., 2019), and natural language processing (Osman & Barukub, 2020; Guillaume, 2021). Due to its combinatorial nature, graph alignment is computationally challenging, often requiring approximation or heuristic algorithms.

Graph alignment methods are typically classified into three categories based on their alignment strategies: optimization-based, optimal transport-based, and embedding-based approaches. They also vary in the level of supervision required, ranging from unsupervised to semi-supervised, using partial node correspondences, and fully supervised methods. A detailed overview of these categories with related works is provided in Appendix A.

Embedding-based graph alignment methods encode graphs into low-dimensional node representations via Graph Neural Networks (GNNs) (He et al., 2024; Fey et al., 2020; Gao et al., 2021b), followed by alignment through transformations or joint learning with cross-graph regularization. Node matching is then performed using nearest-neighbor search or assignment algorithms, achieving better scalability than optimization-based alternatives.

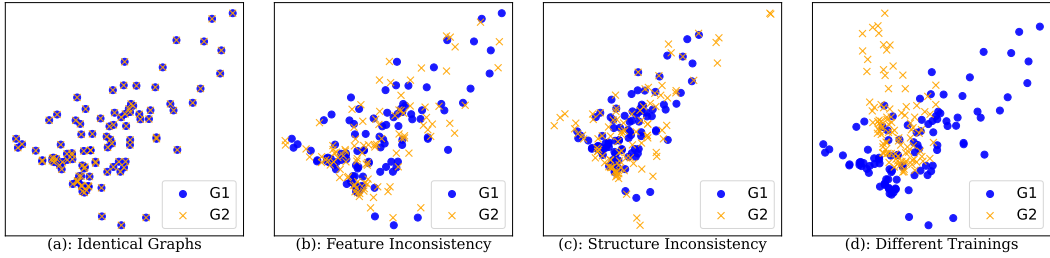


Figure 1: Limitations of embedding-based graph alignment on synthetic data. \mathcal{G}_1 is a ring graph with 100 nodes and 2D random features. (a) \mathcal{G}_2 is identical to \mathcal{G}_1 , yielding well-aligned embeddings. (b) Feature inconsistency introduced through Gaussian noise (std=0.2) causes divergence. (c) Structural inconsistency via 30% edge dropout distorts the embedding alignment. (d) Identical graphs with different training runs show embedding instability, highlighting unsupervised learning limitations.

These methods are typically formulated as unsupervised learning tasks, where ground-truth node correspondences across graphs are unavailable. Despite their computational advantages, these approaches face several inherent challenges that limit their effectiveness and reliability:

1) Degradation of node distinctiveness in GNN embeddings. While GNNs capture structural information by aggregating neighborhood features, this process inherently reduces node distinctiveness. This limitation is particularly problematic for graph alignment, where accurate correspondence identification depends on highly discriminative representations. As embeddings lose uniqueness, alignment becomes increasingly ambiguous and error-prone.

2) Misaligned latent spaces across graphs. In the absence of supervision, explicit constraints, or alignment-specific objectives during training, embedding-based methods struggle to produce comparable latent spaces across different graphs. Even when using shared encoders, the resulting embeddings often occupy misaligned geometric spaces due to structural inconsistencies, feature heterogeneity, and training instability. As illustrated in Figure 1, nodes with identical local structures may be mapped to distant regions in their respective latent spaces.

This misalignment arises from multiple sources. First, structural inconsistencies, such as missing or noisy edges, distort neighborhood aggregation during message passing, leading to incompatible embeddings for otherwise corresponding nodes. Second, feature inconsistency across graphs, stemming from differences in user attributes, schema, or data domains, causes graph encoders to embed semantically equivalent nodes into disjoint subspaces. Lastly, GNN-based encoders often exhibit stochasticity in training; different random initializations can yield drastically different embeddings, even on fixed graph inputs (Moschella et al., 2023). Without explicit mechanisms to harmonize or align the latent spaces, these inconsistencies severely hinder cross-graph communication and undermine the reliability of node alignment.

Figure 1 illustrates the latent spaces learned by a 2-layer GCN on synthetic graphs. Panel (a) shows that identical graphs produce well-aligned embeddings, facilitating effective correspondence detection. However, panels (b) and (c) reveal that minor feature and structural inconsistencies cause corresponding node embeddings to diverge significantly, compromising alignment quality. Most critically, panel (d) shows that retraining the same model on identical graphs with different random initializations produces drastically different latent spaces, underscoring the instability and non-deterministic nature of learned representations.

In this paper, we introduce GADL, **Graph Alignment with Dual-pass encoder and Latent space communication**, which builds upon the Graph Autoencoder (GAE) framework (Kipf & Welling, 2016) by incorporating a dual-pass encoding architecture and cross-graph latent communication mechanism tailored for unsupervised graph alignment tasks.

First, to address the degradation of node distinctiveness caused by oversmoothing in GNN neighborhood aggregation, GADL employs a dual-pass GCN encoder that combines low-pass and high-pass spectral filters. The low-pass branch captures structural context, while the high-pass branch preserves fine-grained node distinctiveness. Their concatenation yields embeddings that are both structure-aware and highly discriminative, crucial for accurate graph alignment. Second, to ad-

dress latent space misalignment across graphs, GADL incorporates a geometry-aware functional map module that learns explicit transformations between different graph embeddings. By enforcing bijectivity and orthogonality constraints, this module ensures that embeddings across graphs become mutually consistent and locally isometric, enabling effective cross-graph communication and alignment without requiring ground-truth node pairs. Our key contributions can be summarized as:

1. We propose a novel dual-pass GCN encoder that combines low-pass and high-pass spectral filters to produce embeddings that are both structure-aware and highly discriminative.
2. We introduce a geometry-aware functional map module that explicitly aligns latent spaces across graphs, enabling robust cross-graph communication without supervision.
3. We conduct extensive experiments on graph alignment benchmarks, demonstrating superior performance and robustness to structural inconsistencies in unsupervised alignment tasks.
4. We evaluate our framework on vision-language benchmarks, demonstrating that our framework effectively generalizes beyond graph domains to enable cross-modal alignment.

2 PRELIMINARIES

We formally define the problem of aligning attributed nodes from a source graph \mathcal{G}_s to a target graph \mathcal{G}_t in an unsupervised setting. The goal is to identify, for each node in the source graph, a corresponding node in the target graph.

Definition 1 (Graph Alignment (GA)). *Given two graphs $\mathcal{G}_s = (\mathcal{V}_s, \mathcal{E}_s, \mathbf{X}_s)$ and $\mathcal{G}_t = (\mathcal{V}_t, \mathcal{E}_t, \mathbf{X}_t)$, where \mathcal{V} denotes the set of nodes, \mathcal{E} the set of edges, and $\mathbf{X}_* \in \mathbb{R}^{N_* \times k_*}$ the associated node attributes (features), the graph alignment problem aims to find a one-to-one mapping $\pi : \mathcal{V}_s \rightarrow \mathcal{V}_t$ such that for each node $u \in \mathcal{V}_s$, $\pi(u) = v \in \mathcal{V}_t$ and $\pi^{-1}(v) = u$. The objective is to identify correspondences between nodes in \mathcal{G}_s and \mathcal{G}_t that preserve structural similarity and attribute consistency across the two graphs.*

We assume the GA problem between two general graphs with different number of nodes ($|\mathcal{V}_s| \neq |\mathcal{V}_t|$) in an unsupervised setting, where no ground-truth node correspondences are available during training, and the alignment depends solely on the structural and attribute information of the graphs.

2.1 GRAPH AUTOENCODER FOR UNSUPERVISED NODE EMBEDDING

Graph autoencoders (GAEs) (Kipf & Welling, 2016) learn node embeddings in an unsupervised setting, generating low-dimensional representations that capture both node features and graph structure. Following the general principle of autoencoders, a GAE consists of two main components: an **encoder** $q_\theta(\mathbf{Z} | \mathcal{G})$ that maps the input graph $\mathcal{G} = (\mathcal{V}, \mathcal{E}, \mathbf{X})$, where $\mathbf{X} \in \mathbb{R}^{|\mathcal{V}| \times k}$, into a latent embedding matrix $\mathbf{Z} \in \mathbb{R}^{|\mathcal{V}| \times d}$, leveraging both graph structure and node features to learn meaningful representations; and a **decoder** $p_\phi(\hat{\mathcal{G}} | \mathbf{Z})$ that reconstructs the original graph structure and node attributes from these latent embeddings, producing an approximation $\hat{\mathcal{G}}$ of the input graph. The model is trained to minimize a loss function composed of a reconstruction loss \mathcal{L}_{rec} , which measures the difference between \mathcal{G} and $\hat{\mathcal{G}}$, and optionally a regularization term \mathcal{L}_{reg} on the latent space:

$$\mathcal{L} = \mathcal{L}_{\text{rec}}(\mathcal{G}, \hat{\mathcal{G}}) + \lambda \mathcal{L}_{\text{reg}}(\mathbf{Z}), \quad (1)$$

where λ controls the strength of regularization. This framework enables unsupervised learning of node embeddings that capture the intrinsic geometric structure of the graph, thereby facilitating downstream tasks such as graph alignment.

In this framework, the encoder is typically implemented using a GNN $\phi(\mathbf{X}, \mathbf{S}; \theta) : \mathbb{R}^{N \times k} \rightarrow \mathbb{R}^{N \times d}$ with parameters θ , which maps node features \mathbf{X} and graph structure \mathbf{S} (e.g., an adjacency or normalized Laplacian matrix) to latent node embeddings \mathbf{Z} . The decoder is typically a simple, non-parametric function that reconstructs the graph structure from the learned embeddings. A common choice is the inner product decoder, which estimates the adjacency matrix $\hat{\mathbf{A}}$ as $\hat{\mathbf{A}} = \mathbf{Z}\mathbf{Z}^\top$. This formulation assumes that the similarity between node embeddings reflects the likelihood of an edge, enabling the reconstruction of the graph topology directly from the embedding space.

2.2 FUNCTIONAL MAP ON GRAPHS

The functional map framework, originally proposed for 3D shape correspondence (Ovsjanikov et al., 2012), offers a compact and flexible approach that converts the problem of finding a complex node-to-node correspondence into learning a small, low-dimensional operator C that aligns functions represented in a spectral basis. This paradigm naturally extends to graphs (Fumero et al., 2025; Behmanesh et al., 2024), where functions are defined on nodes, providing a powerful framework for comparing and aligning graph-structured data.

Building on the general framework of Deep Geometric Functional Maps (Donati et al., 2020), the functional map formulation is adapted to operate on graph-based latent representations through:

1. Feature extraction. Given a pair of graphs \mathcal{G}_1 and \mathcal{G}_2 , each is associated with a set of descriptor functions, denoted by $\mathcal{F}_\theta(\mathcal{G}_1)$ and $\mathcal{F}_\theta(\mathcal{G}_2)$, respectively. A descriptor function is a real-valued function defined on the nodes of a graph, either hand-crafted to capture structural information shared across graphs or learned via neural encoders, producing row feature matrices \mathbf{F}_1 and \mathbf{F}_2 .

2. Projection to spectral domain: For each domain, the spectral basis Φ_* is computed via eigen-decomposition of the normalized graph Laplacian $\mathbf{L} = \mathbf{I} - \mathbf{D}^{-\frac{1}{2}}\mathbf{A}\mathbf{D}^{-\frac{1}{2}}$. Descriptor functions are then projected onto the reduced spectral subspace $\Phi_* \in \mathbb{R}^{n_* \times r}$, spanned by the first r eigenvectors, resulting in the spectral coefficients $\hat{\mathbf{F}}_1 = \Phi_1^\top \mathbf{F}_1$, and $\hat{\mathbf{F}}_2 = \Phi_2^\top \mathbf{F}_2$.

3. Functional map estimation. A functional map $\mathbf{C}_{12} \in \mathbb{R}^{r \times r}$ is then estimated by aligning the spectral descriptors between the two domains via the following regularized least squares objective:

$$\mathbf{C}_{12} = \arg \min_{\mathbf{C}} \|\mathbf{C}\hat{\mathbf{F}}_1 - \hat{\mathbf{F}}_2\|_F^2 + \alpha \|\Lambda_2 \mathbf{C} - \mathbf{C}\Lambda_1\|_F^2, \quad (2)$$

where the second term is the Laplacian commutativity regularizer, enforcing that \mathbf{C}_{12} approximately commutes with the graph Laplacians to preserve spectral properties.

3 METHOD OVERVIEW

As established in the introduction, learning-based frameworks for graph alignment suffer from two fundamental limitations that significantly impair their performance: *loss of node distinctiveness* through feature aggregation and *misaligned latent spaces* in unsupervised cross-graph scenarios. In the following, we present the proposed framework that addresses these challenges through architectural innovations that preserve node distinguishability while enforcing embedding space alignment.

3.1 OVERALL FRAMEWORK

Given two graphs $\mathcal{G}_s = (\mathcal{V}_s, \mathcal{E}_s, \mathbf{X}_s)$ and $\mathcal{G}_t = (\mathcal{V}_t, \mathcal{E}_t, \mathbf{X}_t)$, the framework employs a dual-pass encoder with shared parameters θ to extract meaningful node representations. The encoder processes both graphs simultaneously, generating latent embeddings $\mathbf{Z}_s = f_\theta(\mathbf{X}_s, \mathbf{A}_s) \in \mathbb{R}^{|\mathcal{V}_s| \times d}$ and $\mathbf{Z}_t = f_\theta(\mathbf{X}_t, \mathbf{A}_t) \in \mathbb{R}^{|\mathcal{V}_t| \times d}$ by jointly encoding graph structure and node attributes. To address latent space misalignment, a regularized functional map module enforces structural constraints and enables communication between the embedding spaces. Figure 2 provides a schematic overview.

3.2 GRAPH ENCODER

Given a graph $\mathcal{G} = (\mathcal{V}, \mathcal{E}, \mathbf{X})$, a graph encoder $\mathbf{Z} = f_\theta(\mathbf{X}, \mathbf{A}) \in \mathbb{R}^{|\mathcal{V}| \times d}$ embeds each node $v_i \in \mathcal{V}$ into a latent vector $\mathbf{z}_i \in \mathbb{R}^d$, such that the embeddings of neighboring nodes are encouraged to be similar. While this property allows the encoder to capture the local graph structure effectively, it poses a significant limitation for graph alignment tasks by reducing the distinctiveness of individual nodes, an essential factor for accurately identifying corresponding nodes across graphs.

Definition 2 (Ideal node embedding for graph alignment). *An ideal node embedding for graph alignment achieves two properties: local consistency, where neighboring node embeddings are similar ($\max_{v \in \mathcal{V}} \max_{u \in \mathcal{N}(v)} \|h_v^{(k)} - h_u^{(k)}\|$ is small), and global distinctiveness, where distinct nodes have*

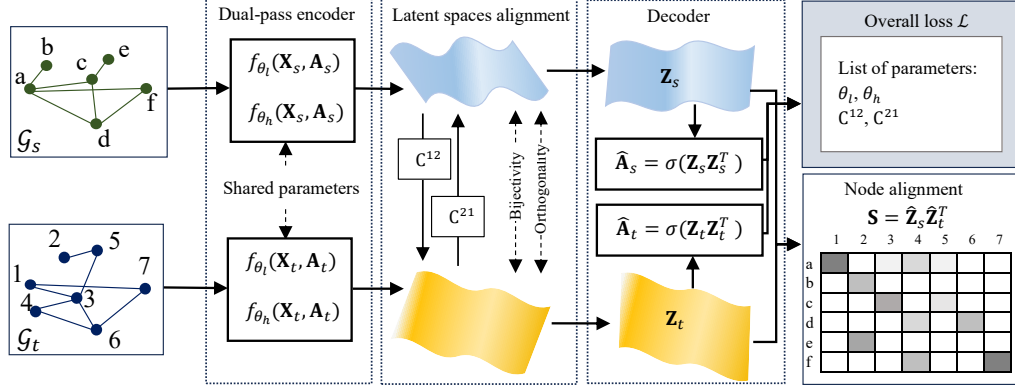


Figure 2: Overview of the proposed framework. Given input graphs, the model uses a dual-pass encoder with shared parameters to extract node embeddings. A regularized functional map module resolves latent space misalignment by enforcing structural constraints and enabling cross-space communication. A graph decoder reconstructs the inputs, and the model is optimized with an overall loss. Finally, alignments are estimated via cosine similarity and greedy matching.

sufficiently different embeddings ($\min_{v,w \in V} \|h_v^{(k)} - h_w^{(k)}\|$ is large). Graph alignment thus requires embedding nodes that balance a fundamental trade-off: preserving local similarities to capture structure while maintaining node distinctiveness for unique identification.

One of the simple yet effective graph encoders is the Graph Convolutional Network (GCN) (Kipf & Welling, 2017), which extends convolution to graph-structured data by aggregating neighboring node information to capture both features and structure. A single GCN layer is defined by $\mathbf{H}^{(l+1)} = \sigma(\tilde{\mathbf{D}}^{-\frac{1}{2}} \tilde{\mathbf{A}} \tilde{\mathbf{D}}^{-\frac{1}{2}} \mathbf{H}^{(l)} \mathbf{W}^{(l)})$, where $\tilde{\mathbf{A}} = \mathbf{A} + \mathbf{I}$ is the adjacency matrix with self-loops, $\tilde{\mathbf{D}}$ is the degree matrix, $\mathbf{H}^{(l)}$ and $\mathbf{W}^{(l)}$ are the feature and weight matrices, and $\sigma(\cdot)$ is the activation function.

Spectral interpretation of GCN: In graph signal processing, the graph Laplacian is defined as $\mathbf{L} = \mathbf{D} - \mathbf{A}$, where \mathbf{D} is the degree matrix and \mathbf{A} is the adjacency matrix. The Laplacian can be decomposed as $\mathbf{L} = \mathbf{U} \mathbf{\Lambda} \mathbf{U}^\top$, where $\mathbf{U} = (\mathbf{u}_1, \dots, \mathbf{u}_n)$ is the matrix of eigenvectors, and $\mathbf{\Lambda} = \text{diag}(\lambda_1, \dots, \lambda_n)$ is the diagonal matrix of eigenvalues. The normalized graph Laplacian is defined as $\mathbf{L}_{\text{sym}} = \mathbf{D}^{-1/2} \mathbf{L} \mathbf{D}^{-1/2}$, whose eigenvalues λ_i lie within the interval $[0, 2]$.

The GCN filter can be expressed as $\tilde{\mathbf{A}}_{\text{GCN,sym}} = \mathbf{I} - \tilde{\mathbf{L}}_{\text{sym}} = \mathbf{U}(\mathbf{I} - \tilde{\mathbf{\Lambda}})\mathbf{U}^\top$, with an associated frequency response function $p_{\text{GCN}}(\tilde{\lambda}_i) = 1 - \tilde{\lambda}_i$. Since the eigenvalues satisfy $\tilde{\lambda}_i \in [0, 2)$, the response function $p_{\text{GCN}}(\tilde{\lambda}_i)$ decreases as $\tilde{\lambda}_i$ increases, particularly over the range $[0, 1]$. This behavior implies that the GCN filter primarily suppresses high-frequency components and thus acts as a low-pass filter in that region. However, for $\tilde{\lambda}_i > 1$, $p_{\text{GCN}}(\tilde{\lambda}_i)$ becomes negative, introducing noise and disrupting smoothness. This means GCN is not a completely low-pass filter and can degrade performance due to this issue.

Node embedding via spectral filtering: Low-pass filters preserve low-frequency components (small λ_i) and suppress high-frequency components, producing smooth embeddings where neighboring nodes have similar representations. Such embeddings are effective at capturing local structure and community information within the graph. In contrast, high-pass filters preserve high-frequency components (large λ_i), emphasizing the differences between neighboring nodes. This leads to embeddings that capture distinctive, discriminative features, making the latent representations of nodes more distinct and farther apart from those of their neighbors.

Dual-pass GCN encoder with spectral filtering: In our proposed model, we design a dual-encoder architecture comprising two complementary GCN variants that exploit the spectral properties of graph signals. The architecture consists of: 1) a low-pass GCN encoder $\mathbf{Z}_l = f_{\theta_l}(\mathbf{X}, \mathbf{A})$ that aggregates information from neighboring nodes, and 2) a high-pass GCN encoder $\mathbf{Z}_h = f_{\theta_h}(\mathbf{X}, \mathbf{A})$, which highlights differences between a node and its neighbors, generating distinctive embeddings

that effectively capture discriminative features. The final node representation is obtained through concatenation $\mathbf{Z} = [\mathbf{Z}_l \parallel \mathbf{Z}_h] \in \mathbb{R}^{|\mathcal{V}| \times (d_l + d_h)}$.

Both encoders employ a unified spectral convolution framework with layer-wise propagation rule:

$$\mathbf{z}_*^{(m+1)} = \sigma \left(\tilde{\mathbf{D}}^{-\frac{1}{2}} \tilde{\mathbf{A}}_* \tilde{\mathbf{D}}^{-\frac{1}{2}} \mathbf{z}_*^{(m)} \mathbf{W}_*^{(m)} \right) \quad (3)$$

where $\tilde{\mathbf{A}}_l = \frac{1}{2} (\tilde{\mathbf{A}} + \tilde{\mathbf{D}})$ for low-pass and $\tilde{\mathbf{A}}_h = \frac{1}{2} (\tilde{\mathbf{D}} - \tilde{\mathbf{A}})$ for high-pass spectral encoding.

The **low-pass graph filter** is characterized by $\tilde{\mathbf{A}}_{l,\text{sym}} = \tilde{\mathbf{D}}^{-1/2} \tilde{\mathbf{A}}_l \tilde{\mathbf{D}}^{-1/2} = \mathbf{I} - \frac{1}{2} \tilde{\mathbf{L}}_{\text{sym}} = \mathbf{U} \left(\mathbf{I} - \frac{1}{2} \tilde{\mathbf{\Lambda}} \right) \mathbf{U}^\top$. This formulation reveals that $\tilde{\mathbf{A}}_{l,\text{sym}}$ exhibits a frequency response $p_l(\tilde{\lambda}_i) = 1 - \frac{1}{2} \tilde{\lambda}_i$. The response function is *monotonically* decreasing over $\tilde{\lambda}_i \in [0, 2]$, thereby attenuating high-frequency components while preserving smooth graph signals. This enables capturing local structural patterns and maintaining graph regularity in embeddings. Similarly, the **high-pass graph filter** is defined by $\tilde{\mathbf{A}}_{h,\text{sym}} = \tilde{\mathbf{D}}^{-1/2} \tilde{\mathbf{A}}_h \tilde{\mathbf{D}}^{-1/2} = \frac{1}{2} \tilde{\mathbf{L}}_{\text{sym}} = \mathbf{U} \left(\frac{1}{2} \tilde{\mathbf{\Lambda}} \right) \mathbf{U}^\top$. This formulation indicates that $\tilde{\mathbf{A}}_{h,\text{sym}}$ acts as a spectral filter with frequency response $p_h(\tilde{\lambda}_i) = \frac{1}{2} \tilde{\lambda}_i$. The response $p_h(\tilde{\lambda}_i)$ *monotonically* increases over $\tilde{\lambda}_i \in [0, 2]$, suppressing low frequencies while amplifying high frequencies, functioning as a high-pass filter (see (Wang et al., 2022a)).

Theorem 1 (Discriminativity of dual-pass GCN encoder). *Let $\mathbf{z}_i^{\text{low}} \in \mathbb{R}^{d_1}$ and $\mathbf{z}_i^{\text{high}} \in \mathbb{R}^{d_2}$ denote node embeddings from low-pass and high-pass GCN encoders, respectively, and dual-pass embedding is defined as the concatenation $\mathbf{z}_i = [\mathbf{z}_i^{\text{low}} \parallel \mathbf{z}_i^{\text{high}}] \in \mathbb{R}^{d_1 + d_2}$. Using this architecture for both graphs \mathcal{G}_1 and \mathcal{G}_2 , the dual-pass GCN encoder provides ideal node embeddings for graph alignment by satisfying:*

1. *Spectral locality preservation: the embedding \mathbf{z}_i preserves neighborhood similarity comparably to $\mathbf{z}_i^{\text{low}}$.*
2. *Enhanced node discriminability: the embedding \mathbf{z}_i provides superior node correspondence discrimination compared to either component alone.*

The proof is provided in Appendix B.

3.3 LATENT SPACE COMMUNICATION

While each GAE independently produces a latent space for its respective graph, resulting in misaligned embeddings, we address this limitation by incorporating deep functional maps to learn explicit mappings between latent representations. Rather than directly comparing raw embeddings, which may differ by arbitrary isometric transformations, we learn functional maps \mathbf{C}^{12} and \mathbf{C}^{21} that transform functions between latent spaces. These maps are optimized within our network using Equation 2, where \mathbf{F}_1 and \mathbf{F}_2 represent embeddings from the shared dual-pass encoder.

To facilitate latent space communication, our framework leverages spectral geometry principles and a regularized functional map module that enforces structural constraints. We impose *bijectivity* and *orthogonality* losses to ensure the maps \mathbf{C}^{12} and \mathbf{C}^{21} are approximately invertible and locally isometric, preserving essential geometric properties. The bijectivity loss promotes invertibility by ensuring functions mapped between latent spaces and back are accurately reconstructed, enforcing structural consistency and mutual alignment. Formally, it is defined as:

$$\mathcal{L}_{\text{bij}} = \|\mathbf{C}_{12} \mathbf{C}_{21} - \mathbf{I}\|_F^2 + \|\mathbf{C}_{21} \mathbf{C}_{12} - \mathbf{I}\|_F^2. \quad (4)$$

The orthogonality loss enforces that functional maps behave as partial isometries, preserving local geometry and structural information during cross-space transformations. This loss is given by:

$$\mathcal{L}_{\text{orth}} = \|\mathbf{C}_{12} \mathbf{C}_{12}^\top - \mathbf{I}\|_F^2 + \|\mathbf{C}_{21}^\top \mathbf{C}_{21} - \mathbf{I}\|_F^2. \quad (5)$$

These regularizations enable *geometry-aware alignment* of latent spaces, facilitating reliable cross-graph alignment without requiring any ground-truth correspondences and effectively bridging independently learned embeddings.

3.4 GRAPH DECODER

Given latent node embeddings $\mathbf{Z} = f_\theta(\mathbf{X}, \mathbf{A}) \in \mathbb{R}^{|V| \times d}$ produced by the encoder, the decoder reconstructs graph structure using inner product operations $\hat{\mathbf{A}}_s = \sigma(\mathbf{Z}_s \mathbf{Z}_s^\top)$, and $\hat{\mathbf{A}}_t = \sigma(\mathbf{Z}_t \mathbf{Z}_t^\top)$, where $\sigma(\cdot)$ denotes the element-wise sigmoid function.

3.5 MODEL OPTIMIZATION AND TRAINING LOSS

Our model jointly optimizes GAE parameters and functional maps \mathbf{C}_{12} , \mathbf{C}_{21} through end-to-end training. Given embeddings $\mathbf{Z}_1 = f_\theta(\mathbf{X}_s, \mathbf{A}_s)$ and $\mathbf{Z}_2 = f_\theta(\mathbf{X}_t, \mathbf{A}_t)$, we project them into spectral domains using graph Laplacian eigenvectors, yielding descriptors $\hat{\mathbf{F}}_1$ and $\hat{\mathbf{F}}_2$. Functional maps $\mathbf{C}_{12} \in \mathbb{R}^{k \times k}$ and $\mathbf{C}_{21} \in \mathbb{R}^{k \times k}$ align these spectral features via:

$$\mathcal{L}_{\text{FM}}^{12} = \alpha \left\| \mathbf{C}_{12} \hat{\mathbf{F}}_1 - \hat{\mathbf{F}}_2 \right\|_F^2 + \beta \left\| \Lambda_2 \mathbf{C}_{12} - \mathbf{C}_{12} \Lambda_1 \right\|_F^2 \quad (6)$$

$$\mathcal{L}_{\text{FM}}^{21} = \alpha \left\| \mathbf{C}_{21} \hat{\mathbf{F}}_2 - \hat{\mathbf{F}}_1 \right\|_F^2 + \beta \left\| \Lambda_1 \mathbf{C}_{21} - \mathbf{C}_{21} \Lambda_2 \right\|_F^2 \quad (7)$$

We incorporate these objectives as differentiable loss terms, with \mathbf{C}_{12} and \mathbf{C}_{21} as trainable parameters optimized end-to-end via backpropagation. These losses are combined with the standard GAE reconstruction loss, minimizing binary cross-entropy between the observed adjacency matrix \mathbf{A} and its reconstruction $\hat{\mathbf{A}}$:

$$\mathcal{L}_{\text{rec}} = \text{BCE}(\mathbf{A}_s, \hat{\mathbf{A}}_s) + \text{BCE}(\mathbf{A}_t, \hat{\mathbf{A}}_t), \quad (8)$$

where $\text{BCE}(\cdot, \cdot)$ denotes the element-wise binary cross-entropy loss. The overall training objective combines the training loss and regularization terms in a weighted sum:

$$\mathcal{L}_{\text{total}} = \mathcal{L}_{\text{rec}} + \lambda_{\text{FM}} (\mathcal{L}_{\text{FM}}^{12} + \mathcal{L}_{\text{FM}}^{21}) + \lambda_{\text{bij}} \mathcal{L}_{\text{bij}} + \lambda_{\text{orth}} \mathcal{L}_{\text{orth}} \quad (9)$$

The entire architecture is trained end-to-end via gradient descent, ensuring that functional maps and embeddings co-evolve to produce structure-aware cross-graph correspondences.

3.6 NODE ALIGNMENT

Given learned embeddings, we compute the cosine similarity matrix $\mathbf{S} = \hat{\mathbf{Z}}_s \hat{\mathbf{Z}}_t^\top$ between ℓ_2 -normalized node embeddings $\hat{\mathbf{Z}}_s, \hat{\mathbf{Z}}_t \in \mathbb{R}^{N \times d}$ from source and target graphs. Node correspondences are predicted using greedy matching, iteratively selecting the highest similarity unmatched pairs until complete one-to-one alignment is achieved.

4 EXPERIMENTS

In this section, we aim to address the following research questions: (1) **robustness**: is GADL more robust to feature and structural inconsistencies than existing state-of-the-art graph alignment methods? (2) **effectiveness**: does GADL outperform state-of-the-art methods on real-world graph alignment tasks? (3) **generalization**: how effectively does GADL generalize to vision-language alignment? (4) **ablation analysis**: what is the contribution of each component in GADL to the overall alignment performance? (5) **encoder evaluation**: how does the proposed *dual-pass GCN encoder* improve node embeddings over standard GNNs? (6) **hyperparameter sensitivity**: how sensitive is GADL to hyperparameter variations?

A comprehensive description of the experimental setup, including benchmarks, baselines, evaluation metrics, and experimental settings, is provided in the Appendix C.

4.1 ROBUSTNESS: EVALUATION ON SEMI-SYNTHETIC BENCHMARKS

To evaluate the robustness of the proposed GADL model under structural inconsistencies, we conduct experiments on six semi-synthetic benchmark datasets following (He et al., 2024), generating perturbed graph pairs with perturbation levels of 0%, 1%, and 5% (setup in Appendix C.3).

Table 1 compares GADL against state-of-the-arts: Netsimile (Berlingerio et al., 2013), Final (Zhang & Tong, 2016), GAlign (Trung et al., 2020), WAlign (Gao et al., 2021a), GAE (Kipf & Welling, 2016), T-GAE(He et al., 2024), and SLOAlign (Tang et al., 2023a). Results show mean matching accuracy and standard deviation across 10 randomly generated target graphs under structural perturbations of 0%, 1%, and 5%. Results for Final, WAlign, and GAE are from He et al. (2024), while GAlign and SLOAlign are reproduced. Entries marked ”-” indicate scalability failures.

Table 1: Robustness evaluation under different structural inconsistency levels (%).

Dataset	Perturb.	NetSimile	Final	GAlign	WAlign	GAE	T-GAE	SLOAlign	GADL
Celegans	0%	72.7 ± 0.9	92.2 ± 1.2	81.67 ± 0.7	88.4 ± 1.6	86.3 ± 1.3	91.0 ± 1.1	91.12 ± 0.2	92.82 ± 0.9
	1%	66.3 ± 3.8	33.2 ± 7.8	66.23 ± 0.8	80.7 ± 3.0	33.2 ± 8.4	86.5 ± 1.1	85.25 ± 0.6	88.07 ± 0.7
	5%	41.1 ± 13.0	10.4 ± 2.7	49.22 ± 1.6	42.4 ± 21.1	6.5 ± 2.4	69.2 ± 2.1	70.05 ± 0.4	71.74 ± 0.2
Arena	0%	94.7 ± 0.3	97.5 ± 0.3	93.02 ± 0.4	97.4 ± 0.5	97.6 ± 0.4	97.8 ± 0.4	96.22 ± 0.5	98.27 ± 0.3
	1%	87.8 ± 1.0	32.5 ± 5.9	87.46 ± 0.6	90.0 ± 3.1	30.1 ± 17.6	96.0 ± 1.0	95.24 ± 0.4	96.86 ± 0.4
	5%	52.3 ± 5.3	7.2 ± 2.6	64.96 ± 1.2	30.4 ± 17.5	1.4 ± 1.4	78.6 ± 2.5	78.5 ± 0.6	80.69 ± 0.4
Douban	0%	46.4 ± 0.4	89.9 ± 0.3	56.50 ± 1.4	90.0 ± 0.4	89.5 ± 0.4	90.1 ± 0.3	88.17 ± 0.3	90.71 ± 0.4
	1%	40.0 ± 1.2	27.8 ± 5.7	51.40 ± 0.5	77.2 ± 4.8	38.3 ± 16.4	87.3 ± 0.4	85.83 ± 1.2	87.94 ± 0.1
	5%	20.7 ± 4.6	7.8 ± 3.0	29.97 ± 2.2	36.6 ± 13.4	0.6 ± 0.3	70.2 ± 2.5	67.42 ± 0.5	69.62 ± 0.1
Cora	0%	73.7 ± 0.4	87.5 ± 0.7	74.15 ± 0.7	87.2 ± 0.4	87.1 ± 0.8	87.5 ± 0.4	87.74 ± 0.6	88.20 ± 0.2
	1%	66.4 ± 1.6	30.0 ± 3.3	68.53 ± 0.4	80.1 ± 1.2	57.9 ± 5.3	85.1 ± 0.5	84.66 ± 0.1	85.30 ± 0.3
	5%	41.2 ± 3.3	6.7 ± 2.8	45.67 ± 0.8	33.4 ± 7.3	9.6 ± 2.7	67.7 ± 1.3	67.8 ± 0.3	68.22 ± 0.2
DBLP	0%	63.7 ± 0.2	85.6 ± 0.2	66.43 ± 0.6	85.6 ± 0.2	85.2 ± 0.3	85.6 ± 0.2	-	85.82 ± 0.0
	1%	55.1 ± 1.7	15.2 ± 3.3	59.00 ± 0.5	73.1 ± 1.6	19.4 ± 0.6	83.3 ± 0.4	-	82.77 ± 0.3
	5%	19.5 ± 4.8	2.7 ± 0.9	38.84 ± 0.2	15.9 ± 8.3	1.4 ± 0.2	60.8 ± 1.9	-	62.49 ± 0.3
Coauthor CS	0%	90.9 ± 0.1	97.6 ± 0.1	92.18 ± 1.5	97.5 ± 0.2	97.6 ± 0.3	97.6 ± 0.1	-	97.76 ± 0.1
	1%	75.2 ± 2.2	13.3 ± 5.0	81.15 ± 0.7	75.2 ± 5.4	49.5 ± 7.8	93.2 ± 0.8	-	93.41 ± 0.6
	5%	26.3 ± 6.0	2.0 ± 0.4	30.41 ± 0.1	11.3 ± 7.5	0.6 ± 0.1	66.0 ± 1.4	-	68.54 ± 1.2

The results yield several key observations: (1) GADL consistently ranks among the top performers across datasets, maintaining high accuracy even with 5% perturbations while baselines show sharp degradation under structural noise. (2) Embedding-based methods (GAE, T-GAE, GAlign, GADL) generally outperform optimal-transport-based methods (Final). SLOAlign, combining learning and optimization, achieves competitive but suboptimal results compared to pure learning-based models.

4.2 EFFECTIVENESS: EVALUATION ON REAL-WORLD BENCHMARKS

We evaluate the effectiveness of the proposed GADL method on two real-world noisy graph datasets with partial node alignment: Douban Online-Offline and ACM-DBLP. These benchmarks involve distinct graphs with partially aligned nodes. Performance is measured using Hit@*k*, the proportion of ground-truth nodes ranked in the top-*k* predictions. Results are reported in Table 2.

Table 2: Performance of graph alignment methods on real-world benchmarks.

Method	ACM-DBLP				Douban Online-Offline			
	Hit@1	Hit@5	Hit@10	Hit@50	Hit@1	Hit@5	Hit@10	Hit@50
NetSimile	2.59	8.32	12.09	26.42	1.07	2.77	4.74	15.03
GAE	8.10	22.50	30.10	45.10	3.30	9.20	14.10	32.10
GAlign	73.26	91.24	95.09	98.37	41.32	62.43	71.37	87.65
WAlign	62.02	81.96	87.31	93.89	36.40	53.94	67.08	85.33
T-GAE	73.89	91.73	95.33	98.22	36.94	60.64	69.77	88.62
SLOAlign	66.04	84.06	87.95	94.65	51.43	53.43	77.73	90.23
GADL	88.63	94.76	96.16	98.41	53.31	73.61	80.67	94.18

The results reveal key insights: (1) GADL consistently achieves the highest alignment accuracy, outperforming all baselines, outperforming all baselines with substantial margins over second-best models (T-GAE on ACM-DBLP, SLOAlign on Douban). (2) Compared to T-GAE, which employs a GIN encoder but lacks latent-space communication, our GADL model demonstrates superior performance through its dual-pass GCN encoder architecture integrated with latent-space communication. (3) Learning-based methods (T-GAE, GADL) outperform optimal-transport approaches (SLOAlign) on larger benchmarks, demonstrating better robustness to structural variations that violate optimal transport assumptions.

Additional experiments on ablation analysis, encoder evaluation, and hyperparameter sensitivity are provided in Appendices D, E, and F.

4.3 GENERALIZATION: EVALUATION ON VISION-LANGUAGE BENCHMARKS

Latent space alignment is a special case of graph alignment, relying only on embeddings without explicit structure. To highlight this generality, we further evaluate our method on vision-language alignment benchmarks, where the task involves aligning latent representations from diverse pretrained vision and language models. We evaluate latent space alignment across multiple benchmarks using representations from diverse pretrained vision and language models. Full experimental details are provided in Appendix C.4.

Table 3 summarizes the vision-language alignment accuracies on four datasets using three pretrained vision models (CLIP (Ramesh et al., 2022), DeiT (Touvron et al., 2021), and DINOv2 (Oquab et al., 2023)) and two pretrained language models from SentenceTransformers library (Reimers & Gurevych, 2019) (all-mpnet-base-v2 and all-roberta-large-v1). Comprehensive results are in the Appendix G. Results on CIFAR-100 and ImageNet-100 are reproduced using official implementations.

Table 3: Vision-language alignment across four datasets using three pretrained vision models (CLIP, DeiT, and DINOv2) and two pretrained language models: Lan. model 1 (all-mpnet-base-v2) and Lan. model 2 (all-roberta-large-v1).

Method	CIFAR-10		CINIC-10		CIFAR-100		ImageNet-100	
	Lan. model 1	Lan. model 2	Lan. model 1	Lan. model 2	Lan. model 1	Lan. model 2	Lan. model 1	Lan. model 2
CLIP - (ViT-L/14@336)								
LocalCKA	25.0 ± 10.5	17.0 ± 15.9	30.0 ± 0.0	4.0 ± 5.0	24.00 ± 1.41	13.67 ± 0.47	8.00 ± 1.41	8.33 ± 0.47
OT	0.0 ± 0.0	10.0 ± 0.0	49.5 ± 2.2	2.0 ± 4.1	1.00 ± 0.00	1.67 ± 0.47	1.33 ± 0.47	1.00 ± 0.00
FAQ	12.0 ± 10.1	0.5 ± 2.2	30.5 ± 2.2	0.0 ± 0.0	2.33 ± 1.25	2.67 ± 1.70	4.33 ± 1.70	2.33 ± 1.25
MPOpt	0.0 ± 0.0	0.0 ± 0.0	0.0 ± 0.0	0.0 ± 0.0	1.67 ± 1.25	2.67 ± 1.25	4.67 ± 2.05	2.67 ± 0.47
Gurobi	20.5 ± 6.0	47.0 ± 7.3	50.0 ± 0.0	80.0 ± 0.0	2.11 ± 1.29	3.44 ± 1.27	3.22 ± 2.35	4.50 ± 1.50
Hahn-Grant	25.0 ± 10.5	47.0 ± 7.3	50.0 ± 0.0	80.0 ± 0.0	2.33 ± 1.25	3.00 ± 2.16	4.93 ± 2.05	4.67 ± 1.70
GADL	76.7 ± 4.7	73.3 ± 4.7	76.7 ± 4.7	80.0 ± 0.0	79.7 ± 2.0	81.00 ± 1.4	41.3 ± 8.2	45.3 ± 14.2
DeiT - (DeiT-B/16d@384)								
LocalCKA	24.0 ± 9.9	20.0 ± 5.6	68.0 ± 8.9	0.0 ± 0.0	10.33 ± 0.94	23.33 ± 0.47	8.33 ± 1.70	9.33 ± 0.47
OT	12.0 ± 4.1	10.0 ± 0.0	20.0 ± 0.0	0.0 ± 0.0	2.33 ± 0.94	1.67 ± 0.47	2.00 ± 0.00	0.67 ± 0.47
FAQ	40.0 ± 15.2	22.5 ± 9.7	55.5 ± 5.1	0.0 ± 0.0	4.33 ± 0.47	1.33 ± 1.25	3.67 ± 0.47	3.33 ± 0.94
MPOpt	0.0 ± 0.0	0.0 ± 0.0	0.0 ± 0.0	0.0 ± 0.0	0.33 ± 0.47	0.67 ± 0.94	2.67 ± 2.36	1.00 ± 0.82
Gurobi	28.5 ± 3.7	59.0 ± 3.1	10.0 ± 0.0	40.0 ± 0.0	3.67 ± 2.49	3.11 ± 1.91	3.56 ± 1.57	3.00 ± 1.00
Hahn-Grant	28.5 ± 3.7	59.0 ± 3.1	10.0 ± 0.0	40.0 ± 0.0	1.33 ± 0.47	5.33 ± 1.25	1.67 ± 2.36	1.33 ± 1.25
GADL	100.0 ± 0.0	100.0 ± 0.0	100.0 ± 0.0	100.0 ± 0.0	47.3 ± 8.9	42.7 ± 6.3	67.3 ± 4.5	65.7 ± 0.9
DINOv2 - (ViT-G/14)								
LocalCKA	37.5 ± 28.8	18.5 ± 29.2	52.5 ± 31.1	57.0 ± 13.4	4.00 ± 0.82	4.67 ± 0.94	5.33 ± 0.47	6.00 ± 0.82
OT	30.0 ± 13.8	33.5 ± 19.8	77.5 ± 6.4	15.5 ± 7.6	1.00 ± 0.00	1.00 ± 0.00	1.00 ± 0.00	0.33 ± 0.47
FAQ	37.5 ± 21.2	38.0 ± 29.8	31.0 ± 4.5	29.5 ± 2.2	4.33 ± 0.94	3.33 ± 1.25	3.00 ± 0.82	4.33 ± 2.05
MPOpt	73.5 ± 17.9	94.0 ± 18.5	79.0 ± 3.1	47.0 ± 46.0	1.33 ± 1.25	0.33 ± 0.47	4.00 ± 0.82	0.67 ± 0.47
Gurobi	69.5 ± 24.2	100.0 ± 0.0	79.0 ± 3.1	100.0 ± 0.0	2.56 ± 1.64	1.78 ± 1.31	1.50 ± 0.50	2.50 ± 0.50
Hahn-Grant	69.5 ± 24.2	100.0 ± 0.0	79.0 ± 3.1	100.0 ± 0.0	4.00 ± 0.82	2.00 ± 1.41	6.33 ± 0.47	1.22 ± 0.92
GADL	100.0 ± 0.0	100.0 ± 0.0	100.0 ± 0.0	100.0 ± 0.0	67.7 ± 1.7	58.3 ± 0.4	44.3 ± 8.3	49.3 ± 0.4

The results highlight key insights. (1) GADL consistently outperforms all baselines, demonstrating substantial benefits beyond optimization and optimal transport frameworks. (2) Most baselines achieve near-chance accuracies ($\leq 10\%$) with occasional inconsistent successes, even sophisticated solvers like Gurobi fail in certain settings. Performance gaps with GADL become pronounced on challenging benchmarks (CIFAR-100, ImageNet-100), highlighting limitations of treating alignment as pure assignment optimization. (3) Pretrained model choice critically impacts performance, while DINOv2 and DeiT excel on smaller datasets, CLIP consistently outperforms on larger benchmarks.

5 CONCLUSION

We present GADL, a novel framework for unsupervised graph alignment that combines dual-pass encoding with geometry-aware latent space communication. Comprehensive experiments demonstrate consistent performance gains across diverse benchmarks, with successful application to vision-language tasks validating the broader utility of the framework beyond traditional graph domains. While promising, our approach incurs modest computational overhead from dual-pass encoding compared to standard GCN and requires careful hyperparameter tuning. Future work will focus on adaptive spectral filtering and efficient embedding strategies, with potential extensions to molecular networks, social graphs, and multi-modal alignment tasks, including a more thorough evaluation on vision-language benchmarks.

REFERENCES

- Hyojin Bahng, Caroline Chan, Fredo Durand, and Phillip Isola. Cycle consistency as reward: Learning image-text alignment without human preferences. In *Proceedings of the IEEE/CVF International Conference on Computer Vision (ICCV)*, pp. 2116, 2025. doi: 10.48550/arXiv.2506.02095.
- Maysam Behmanesh, Maximilian Krahn, and Maks Ovsjanikov. TIDE: Time derivative diffusion for deep learning on graphs. In Andreas Krause, Emma Brunskill, Kyunghyun Cho, Barbara Engelhardt, Sivan Sabato, and Jonathan Scarlett (eds.), *Proceedings of the 40th International Conference on Machine Learning*, volume 202 of *Proceedings of Machine Learning Research*, pp. 2015–2030. PMLR, 23–29 Jul 2023.
- Maysam Behmanesh, Peyman Adibi, Jocelyn Chanussot, and Sayyed Mohammad Saeed Ehsani. Cross-modal and multimodal data analysis based on functional mapping of spectral descriptors and manifold regularization. *Neurocomputing*, 598:128062, 2024. ISSN 0925-2312. doi: <https://doi.org/10.1016/j.neucom.2024.128062>.
- Michele Berlingerio, Danai Koutra, Tina Eliassi-Rad, and Christos Faloutsos. Network similarity via multiple social theories. In *Proceedings of the 2013 IEEE/ACM International Conference on Advances in Social Networks Analysis and Mining, ASONAM '13*, pp. 1439–1440, New York, NY, USA, 2013. Association for Computing Machinery. ISBN 9781450322409. doi: 10.1145/2492517.2492582.
- Mathilde Caron, Hugo Touvron, Ishan Misra, Hervé Jégou, Julien Mairal, Piotr Bojanowski, and Armand Joulin. Emerging properties in self-supervised vision transformers. In *Proceedings of the IEEE/CVF International Conference on Computer Vision (ICCV)*, pp. 9650–9660, October 2021.
- Wenting Chen, Jie Liu, Tianming Liu, and Yixuan Yuan. Bi-vlgm: Bi-level class-severity-aware vision-language graph matching for text guided medical image segmentation. *International Journal of Computer Vision*, 133(3):1375–1391, 2025. doi: 10.1007/s11263-024-02246-w.
- Luke N Darlow, Elliot J Crowley, Antreas Antoniou, and Amos J Storkey. Cinic-10 is not imagenet or cifar-10. *arXiv preprint arXiv:1810.03505*, 2018.
- Nicolas Donati, Abhishek Sharma, and Maks Ovsjanikov. Deep geometric functional maps: Robust feature learning for shape correspondence. In *2020 IEEE/CVF Conference on Computer Vision and Pattern Recognition (CVPR)*, pp. 8589–8598, 2020. doi: 10.1109/CVPR42600.2020.00862.
- M. Fey, J. E. Lenssen, C. Morris, J. Masci, and N. M. Kriege. Deep graph matching consensus. In *International Conference on Learning Representations (ICLR)*, 2020.
- Marco Fumero, Marco Pegoraro, Valentino Maiorca, Francesco Locatello, and Emanuele Rodolà. Latent functional maps: a spectral framework for representation alignment. In *Proceedings of the 38th International Conference on Neural Information Processing Systems, NIPS '24*, Red Hook, NY, USA, 2025. Curran Associates Inc. ISBN 9798331314385.
- Ji Gao, Xiao Huang, and Jundong Li. Unsupervised graph alignment with wasserstein distance discriminator. In *Proceedings of the 27th ACM SIGKDD Conference on Knowledge Discovery & Data Mining*, pp. 426–435, 2021a.
- Quankai Gao, Fudong Wang, Nan Xue, Jin-Gang Yu, and Guisong Xia. Deep graph matching under quadratic constraint. *2021 IEEE/CVF Conference on Computer Vision and Pattern Recognition (CVPR)*, pp. 5067–5074, 2021b.
- Bruno Guillaume. Graph matching and graph rewriting: GREW tools for corpus exploration, maintenance and conversion. In Dimitra Gkatzia and Djamé Seddah (eds.), *Proceedings of the 16th Conference of the European Chapter of the Association for Computational Linguistics: System Demonstrations*, pp. 168–175, Online, April 2021. Association for Computational Linguistics. doi: 10.18653/v1/2021.eacl-demos.21.
- Gurobi Optimization, LLC. *Gurobi Optimizer Reference Manual*, 2023. URL <https://www.gurobi.com>.

- Doron Haviv, Russell Zhang Kunes, Thomas Dougherty, Cassandra Burdziak, Tal Nawy, Anna Gilbert, and Dana Pe'er. Wasserstein wormhole: scalable optimal transport distance with transformer. In *Proceedings of the 41st International Conference on Machine Learning, ICML'24*. JMLR.org, 2024.
- Jiashu He, Charilaos I. Kanatsoulis, and Alejandro Ribeiro. T-gae: Transferable graph autoencoder for network alignment, 2024.
- Mark Heimann, Haoming Shen, Tara Safavi, and Danai Koutra. REGAL: representation learning-based graph alignment. In *Proceedings of the 27th ACM International Conference on Information and Knowledge Management, CIKM 2018, Torino, Italy, October 22-26, 2018*, pp. 117–126. ACM, 2018.
- Lisa Hutschenreiter, Stefan Haller, Lorenz Feineis, Carsten Rother, Dagmar Kainmüller, and Bogdan Savchynskyy. Fusion moves for graph matching. In *Proceedings of the IEEE/CVF International Conference on Computer Vision (ICCV)*, pp. 6270–6279, October 2021.
- Rishi Jha, Collin Zhang, Vitaly Shmatikov, and John X. Morris. Harnessing the universal geometry of embeddings, 2025.
- Thomas Kipf and Max Welling. Variational graph auto-encoders. *ArXiv*, abs/1611.07308, 2016.
- Thomas N. Kipf and Max Welling. Semi-supervised classification with graph convolutional networks. In *International Conference on Learning Representations (ICLR)*, 2017.
- Nitish Korula and Silvio Lattanzi. An efficient reconciliation algorithm for social networks. *Proc. VLDB Endow.*, 7(5):377–388, January 2014. ISSN 2150-8097. doi: 10.14778/2732269.2732274.
- Danai Koutra, Hanghang Tong, and David Lubensky. Big-align: Fast bipartite graph alignment. In *2013 IEEE 13th International Conference on Data Mining*, pp. 389–398, 2013. doi: 10.1109/ICDM.2013.152.
- Alex Krizhevsky, Geoffrey Hinton, et al. Learning multiple layers of features from tiny images. 2009.
- Jérôme Kunegis. Konect: the koblenz network collection. In *Proceedings of the 22nd International Conference on World Wide Web, WWW '13 Companion*, pp. 1343–1350, New York, NY, USA, 2013. Association for Computing Machinery. ISBN 9781450320382. doi: 10.1145/2487788.2488173.
- Jure Leskovec and Andrej Krevl. SNAP Datasets: Stanford large network dataset collection. <http://snap.stanford.edu/data>, June 2014.
- Chaozhuo Li, Senzhang Wang, Philip S. Yu, Lei Zheng, Xiaoming Zhang, Zhoujun Li, and Yanbo Liang. Distribution distance minimization for unsupervised user identity linkage. *CIKM '18*, pp. 447–456, New York, NY, USA, 2018. Association for Computing Machinery. ISBN 9781450360142. doi: 10.1145/3269206.3271675.
- Chuan-Sheng Liao, Kevin Lu, Michael Baym, Rohit Singh, and Bonnie Berger. Isorankn: spectral methods for global alignment of multiple protein networks. *Bioinformatics*, 25(12):i253–i258, 2009.
- Chang Liu, Shaofeng Zhang, Xiaokang Yang, and Junchi Yan. Self-supervised learning of visual graph matching. In Shai Avidan, Gabriel Brostow, Moustapha Cissé, Giovanni Maria Farinella, and Tal Hassner (eds.), *Computer Vision – ECCV 2022*, pp. 370–388, Cham, 2022a. Springer Nature Switzerland. ISBN 978-3-031-20050-2.
- Zhuang Liu, Hanzi Mao, Chao-Yuan Wu, Christoph Feichtenhofer, Trevor Darrell, and Saining Xie. A convnet for the 2020s. In *Proceedings of the IEEE/CVF conference on computer vision and pattern recognition*, pp. 11976–11986, 2022b.
- Mayug Maniparambil, Raiymbek Akshulakov, Yasser Abdelaziz Dahou Djilali, Mohamed El Amine Seddik, Sanath Narayan, Karttikeya Mangalam, and Noel E. O'Connor. Do vision and language encoders represent the world similarly? In *Proceedings of the IEEE/CVF Conference on Computer Vision and Pattern Recognition (CVPR)*, pp. 14334–14343, June 2024.

- Luca Moschella, Valentino Maiorca, Marco Fumero, Antonio Norelli, Francesco Locatello, and Emanuele Rodolà. Relative representations enable zero-shot latent space communication. In *The Eleventh International Conference on Learning Representations*, 2023.
- Maxime Oquab, Timothée Darcet, Théo Moutakanni, Huy Vo, Marc Szafraniec, Vasil Khalidov, Pierre Fernandez, Daniel Haziza, Francisco Massa, Alaaeldin El-Nouby, et al. Dinov2: Learning robust visual features without supervision. *arXiv preprint arXiv:2304.07193*, 2023.
- Ahmed Hamza Osman and Omar Mohammed Barukub. Graph-based text representation and matching: A review of the state of the art and future challenges. *IEEE Access*, 8:87562–87583, 2020. doi: 10.1109/ACCESS.2020.2993191.
- Maks Ovsjanikov, Mirela Ben-Chen, Justin Solomon, Adrian Butscher, and Leonidas Guibas. Functional maps: a flexible representation of maps between shapes. *ACM Trans. Graph.*, 31(4), July 2012. ISSN 0730-0301. doi: 10.1145/2185520.2185526.
- Shirui Pan, Jia Wu, Xingquan Zhu, Chengqi Zhang, and Yang Wang. Tri-party deep network representation. In *International Joint Conference on Artificial Intelligence 2016*, pp. 1895–1901. Association for the Advancement of Artificial Intelligence (AAAI), 2016.
- Gabriel Peyré, Marco Cuturi, and Justin Solomon. Gromov-wasserstein averaging of kernel and distance matrices. In Maria Florina Balcan and Kilian Q. Weinberger (eds.), *Proceedings of The 33rd International Conference on Machine Learning*, volume 48 of *Proceedings of Machine Learning Research*, pp. 2664–2672, New York, New York, USA, 20–22 Jun 2016. PMLR.
- Aditya Ramesh, Prafulla Dhariwal, Alex Nichol, Casey Chu, and Mark Chen. Hierarchical text-conditional image generation with clip latents. *arXiv preprint arXiv:2204.06125*, 1(2):3, 2022.
- Nils Reimers and Iryna Gurevych. Sentence-bert: Sentence embeddings using siamese bert-networks. *arXiv preprint arXiv:1908.10084*, 2019.
- Olga Russakovsky, Jia Deng, Hao Su, Jonathan Krause, Sanjeev Satheesh, Sean Ma, Zhiheng Huang, Andrej Karpathy, Aditya Khosla, Michael Bernstein, et al. Imagenet large scale visual recognition challenge. *International journal of computer vision*, 115(3):211–252, 2015.
- Dominik Schnaus, Nikita Araslanov, and Daniel Cremers. It’s a (blind) match! towards vision-language correspondence without parallel data. In *Proceedings of the IEEE/CVF Conference on Computer Vision and Pattern Recognition*, 2025.
- Prithviraj Sen, Galileo Namata, Mustafa Bilgic, Lise Getoor, Brian Galligher, and Tina Eliassi-Rad. Collective classification in network data. *AI magazine*, 29(3):93–93, 2008.
- Rohit Singh, Jinbo Xu, and Bonnie Berger. Pairwise global alignment of protein interaction networks by matching neighborhood topology. In Terry Speed and Haiyan Huang (eds.), *Research in Computational Molecular Biology*, pp. 16–31, Berlin, Heidelberg, 2007. Springer Berlin Heidelberg.
- Rohit Singh, Jinbo Xu, and Bonnie Berger. Global alignment of multiple protein interaction networks with application to functional orthology detection. *Proceedings of the National Academy of Sciences*, 105(35):12763–12768, 2008. doi: 10.1073/pnas.0806627105.
- Arnab Sinha, Zhihong Shen, Yang Song, Hao Ma, Darrin Eide, Bo-June Hsu, and Kuansan Wang. An overview of microsoft academic service (mas) and applications. In *Proceedings of the 24th international conference on world wide web*, pp. 243–246, 2015.
- Jianheng Tang, Weiqi Zhang, Jiajin Li, Kangfei Zhao, Fugee Tsung, and Jia Li. Robust attributed graph alignment via joint structure learning and optimal transport. In *2023 IEEE 39th International Conference on Data Engineering (ICDE)*, pp. 1638–1651, 2023a. doi: 10.1109/ICDE55515.2023.00129.
- Jianheng Tang, Kangfei Zhao, and Jia Li. A fused Gromov-Wasserstein framework for unsupervised knowledge graph entity alignment. In Anna Rogers, Jordan Boyd-Graber, and Naoaki Okazaki (eds.), *Findings of the Association for Computational Linguistics: ACL 2023*, pp. 3320–3334, Toronto, Canada, July 2023b. Association for Computational Linguistics. doi: 10.18653/v1/2023.findings-acl.205.

- Hugo Touvron, Matthieu Cord, Matthijs Douze, Francisco Massa, Alexandre Sablayrolles, and Hervé Jégou. Training data-efficient image transformers & distillation through attention. In *International conference on machine learning*, pp. 10347–10357. PMLR, 2021.
- Huynh Thanh Trung, Tong Van Vinh, Nguyen Thanh Tam, Hongzhi Yin, Matthias Weidlich, and Nguyen Quoc Viet Hung. Adaptive network alignment with unsupervised and multi-order convolutional networks. In *2020 IEEE 36th International Conference on Data Engineering (ICDE)*, pp. 85–96. IEEE, 2020.
- Joshua T. Vogelstein, John M. Conroy, Vince Lyzinski, Louis J. Podrazik, Steven G. Kratzer, Eric T. Harley, Donniell E. Fishkind, R. Jacob Vogelstein, and Carey E. Priebe. Fast approximate quadratic programming for graph matching. *PLOS ONE*, 10(4):1–17, 04 2015. doi: 10.1371/journal.pone.0121002.
- Jie Wang, Jiye Liang, Kaixuan Yao, Jianqing Liang, and Dianhui Wang. Graph convolutional autoencoders with co-learning of graph structure and node attributes. *Pattern Recognition*, 121: 108215, 2022a. ISSN 0031-3203. doi: <https://doi.org/10.1016/j.patcog.2021.108215>.
- Tao Wang, Haibin Ling, Congyan Lang, Songhe Feng, and Xiaohui Hou. Deformable surface tracking by graph matching. In *2019 IEEE/CVF International Conference on Computer Vision (ICCV)*, pp. 901–910, 2019. doi: 10.1109/ICCV.2019.00099.
- Yejiang Wang, Yuhai Zhao, Daniel Zhengkui Wang, and Ling Li. Galopa: Graph transport learning with optimal plan alignment. In A. Oh, T. Naumann, A. Globerson, K. Saenko, M. Hardt, and S. Levine (eds.), *Advances in Neural Information Processing Systems*, volume 36, pp. 9117–9130. Curran Associates, Inc., 2023.
- Yinghui Wang, Wenjun Wang, Zixu Zhen, Qiyao Peng, Pengfei Jiao, Wei Liang, Minglai Shao, and Yueheng Sun. Geometry interaction network alignment. *Neurocomputing*, 501:618–628, 2022b. ISSN 0925-2312. doi: <https://doi.org/10.1016/j.neucom.2022.06.077>.
- Keyulu Xu, Weihua Hu, Jure Leskovec, and Stefanie Jegelka. How powerful are graph neural networks? *arXiv preprint arXiv:1810.00826*, 2018a.
- Keyulu Xu, Chengtao Li, Yonglong Tian, Tomohiro Sonobe, Ken-ichi Kawarabayashi, and Stefanie Jegelka. Representation learning on graphs with jumping knowledge networks. In Jennifer G. Dy and Andreas Krause (eds.), *Proceedings of the 35th International Conference on Machine Learning, ICML 2018, Stockholmsmässan, Stockholm, Sweden, July 10-15, 2018*, volume 80 of *Proceedings of Machine Learning Research*, pp. 5449–5458. PMLR, 2018b.
- Zhichen Zeng, Si Zhang, Yinglong Xia, and Hanghang Tong. Parrot: Position-aware regularized optimal transport for network alignment. In *Proceedings of the ACM Web Conference 2023, WWW '23*, pp. 372–382, New York, NY, USA, 2023. Association for Computing Machinery. ISBN 9781450394161. doi: 10.1145/3543507.3583357.
- Si Zhang and Hanghang Tong. Final: Fast attributed network alignment. In *Proceedings of the 22nd ACM SIGKDD international conference on knowledge discovery and data mining*, pp. 1345–1354, 2016.
- Si Zhang and Hanghang Tong. Attributed network alignment: Problem definitions and fast solutions. *IEEE Transactions on Knowledge and Data Engineering*, 31(9):1680–1692, 2018.
- Si Zhang, Hanghang Tong, Long Jin, Yinglong Xia, and Yunsong Guo. Balancing consistency and disparity in network alignment. In *Proceedings of the 27th ACM SIGKDD Conference on Knowledge Discovery & Data Mining, KDD '21*, pp. 2212–2222, New York, NY, USA, 2021. Association for Computing Machinery. ISBN 9781450383325. doi: 10.1145/3447548.3467331.

A RELATED WORK

Extensive research has addressed the graph alignment problem, with existing methods broadly categorized into three families based on their alignment strategies: optimization-based, optimal transport-based, and embedding-based approaches. These methods also differ in terms of the level of supervision required, ranging from unsupervised techniques to semi-supervised methods (which rely on partially paired nodes), and fully supervised approaches.

Traditional graph alignment methods formulate the problem as an optimization task, typically as a Quadratic Assignment Problem (QAP), seeking node permutations that minimize discrepancies between source and target adjacency matrices. IsoRank (Singh et al., 2008) represents a seminal approach, employing a PageRank-inspired algorithm to compute node similarity matrices based on neighbor similarity for unsupervised alignment. BigAlign (Koutra et al., 2013) extends this framework by incorporating both structural and attribute information to enhance alignment accuracy. FINAL (Zhang & Tong, 2016) addresses scalability through matrix factorization, combining global structural consistency with partial anchor constraints.

These optimization-based approaches often struggle with scalability due to the NP-hard nature of QAP, though approximation strategies and relaxations can make them tractable on medium-sized networks. While primarily unsupervised, they can accommodate semi-supervised settings by incorporating known anchor pairs as hard or soft constraint

Optimal transport-based methods model each graph as a probability distribution over its nodes and seek a transport plan, i.e., a soft correspondence, that minimizes a divergence such as the Wasserstein or Gromov-Wasserstein distance between the distributions. This framework offers a principled approach to graph alignment by optimizing the transport cost between node distributions. Unlike the hard alignments produced by QAP-based methods, optimal transport typically yields soft alignment matrices, allowing for uncertainty and partial correspondences.

A notable early contribution in this category is WAlign (Gao et al., 2021a), which jointly learns node embeddings and alignments by minimizing Wasserstein distance between graphs in a shared embedding space using a lightweight GCN and Wasserstein distance discriminator. Building on this direction, FGW (Tang et al., 2023b) employs Fused Gromov-Wasserstein distance to jointly align structural and attribute information through a coarse-to-fine matching scheme. PARROT (Zeng et al., 2023) extends this idea by running Random Walk with Restart (RWR) on both individual graphs and their Cartesian product, capturing more nuanced structural correspondence. GALOPA (Wang et al., 2023) integrates a GNN encoder with a self-supervised OT loss, jointly learning features and transport plans. To improve scalability, Wasserstein Wormhole (Haviv et al., 2024) introduces a transformer-based autoencoder that maps distributions into a latent space where Euclidean distances approximate Wasserstein distances, enabling efficient, linear-time graph comparisons.

These methods are typically unsupervised and particularly effective for noisy or incomplete graphs due to their probabilistic formulation and global alignment perspective.

Embedding-based methods learn vector representations for nodes in each graph and align them based on embedding similarity. This approach typically involves generating node embeddings, either independently or jointly, followed by alignment through nearest-neighbor search or learned mapping functions.

NetSimile (Berlingerio et al., 2013) represents an early embedding-based approach that uses hand-crafted structural features (degree, clustering coefficient) to represent nodes and aligns graphs through direct feature vector comparison using similarity measures. GAlign (Trung et al., 2020) adopts an unsupervised approach where both graphs are independently encoded using a shared Graph Convolutional Network, with node embeddings aligned by minimizing distributional discrepancies such as Wasserstein distance between embedding spaces. NeXtAlign (Zhang et al., 2021) enhances representation learning through a cross-graph attention mechanism that enables nodes in one graph to attend to features in the other. This produces alignment-aware embeddings and improves performance in semi-supervised settings with known anchor node pairs. REGAL (Heimann et al., 2018) generates compact node embeddings by extracting structural features like node degree and local neighborhoods, then aligns nodes across graphs by matching their embeddings based on distance, enabling efficient and scalable graph alignment. GINA (Wang et al., 2022b) addresses hierarchical alignment by projecting node embeddings from Euclidean to hyperbolic space, learn-

ing linear transformations between geometries using anchor nodes to better capture scale-free and hierarchical structures in social and biological networks.

A foundational approach to embedding-based graph learning is the Graph Autoencoder (GAE) and its probabilistic extension, the Variational Graph Autoencoder (VGAE) (Kipf & Welling, 2016). These models use a GCN encoder to generate latent node embeddings, which are then used to reconstruct the adjacency matrix via an inner product decoder. Although originally designed for link prediction, GAEs have become a common backbone for alignment tasks due to their ability to capture global graph structure in an unsupervised manner. Expanding on this foundation, T-GAE (He et al., 2024) addresses scalability through a transferable graph autoencoder trained on small graph families that generalizes to large, unseen networks without fine-tuning. This design enables strong alignment performance while significantly reducing training time and computational overhead. However, typical embedding-based methods often become unstable when graphs differ significantly in structure. SLOAlign (Tang et al., 2023a) is developed to tackle the structure and feature inconsistencies commonly found in these embedding-based graph alignment methods. It formulates alignment as an optimal transport problem on learned intra-graph similarity matrices, combining optimal transport with embedding-based approaches.

B PROOF OF THEOREM 1

Proof. Preliminary Definitions: Let GCN filter $\tilde{\mathbf{A}}_{\text{GCN,sym}} = \mathbf{I} - \tilde{\mathbf{L}}_{\text{sym}} = \mathbf{U}(\mathbf{I} - \tilde{\mathbf{\Lambda}})\mathbf{U}^\top$, where $\mathbf{U} = [\mathbf{u}_1, \dots, \mathbf{u}_n]$ is the eigenbasis, $\tilde{\mathbf{\Lambda}} = \text{diag}(\hat{\lambda}_1, \dots, \hat{\lambda}_n)$ is the diagonal matrix of eigenvalues, and each eigenvalue satisfies $\hat{\lambda}_i \in [0, 2]$. The spectral representation of node features is: $\mathbf{X} = \sum_{k=1}^n \hat{\mathbf{X}}_k \mathbf{u}_k$, where $\hat{\mathbf{X}}_k = \mathbf{u}_k^\top \mathbf{X}$.

- The low-pass component captures the smooth, global structure of the graph. It aggregates information from neighbors, producing embeddings: $\mathbf{Z}_{\text{low}} = \sum_{k=1}^n p_{\text{low}}(\hat{\lambda}_k) \hat{\mathbf{X}}_k \mathbf{u}_k$, where $p_{\text{low}}(\hat{\lambda}_k) = 1 - \frac{1}{2}\hat{\lambda}_k$. This captures smoothed signals over the graph, node embeddings are averages of their neighbors.
- The high-pass component captures complementary, local variations and finer structural details, given by: $\mathbf{Z}_{\text{high}} = \sum_{k=1}^n p_{\text{high}}(\hat{\lambda}_k) \hat{\mathbf{X}}_k \mathbf{u}_k$, where $p_{\text{high}}(\hat{\lambda}_k) = \frac{1}{2}\hat{\lambda}_k$.

Claim 1 (Neighborhood preservation). The dual-pass embedding \mathbf{z}_i preserves neighborhood similarity as effectively as the low-pass embedding $\mathbf{z}_i^{\text{low}}$.

Proof of Claim 1. The key insight underlying local consistency is that neighborhood similarity is primarily encoded in low-frequency spectral components, which capture smooth variations across connected nodes.

For the dual-pass embeddings of nodes i and j , the cosine similarity can be written as:

$$\langle \mathbf{z}_i, \mathbf{z}_j \rangle = \langle \mathbf{z}_i^{\text{low}}, \mathbf{z}_j^{\text{low}} \rangle + \langle \mathbf{z}_i^{\text{high}}, \mathbf{z}_j^{\text{high}} \rangle + \langle \mathbf{z}_i^{\text{low}}, \mathbf{z}_j^{\text{high}} \rangle + \langle \mathbf{z}_i^{\text{high}}, \mathbf{z}_j^{\text{low}} \rangle.$$

The filters are designed to be spectrally complementary,

$$p_{\text{low}}(\hat{\lambda}_k) + p_{\text{high}}(\hat{\lambda}_k) = (1 - \frac{1}{2}\hat{\lambda}_k) + \frac{1}{2}\hat{\lambda}_k = 1, \quad \forall \hat{\lambda}_k \in [0, 2].$$

Due to their complementary spectral responses, the low-pass and high-pass components are approximately orthogonal. To see this, note that the low-pass filter $p_{\text{low}}(\hat{\lambda}_k) = 1 - \frac{1}{2}\hat{\lambda}_k$ is monotonically decreasing, achieving maximum response at $\hat{\lambda}_k = 0$ and minimum at $\hat{\lambda}_k = 2$. Conversely, the high-pass filter $p_{\text{high}}(\hat{\lambda}_k) = \frac{1}{2}\hat{\lambda}_k$ is monotonically increasing, with minimum response at $\hat{\lambda}_k = 0$ and maximum at $\hat{\lambda}_k = 2$. The spectral overlap between components is measured by the product $p_{\text{low}}(\hat{\lambda}_k) \cdot p_{\text{high}}(\hat{\lambda}_k) = \frac{1}{4}\hat{\lambda}_k(2 - \hat{\lambda}_k)$, which is maximized only at the intermediate eigenvalue $\hat{\lambda}_k = 1$ and approaches zero at both extremes.

This spectral disjointness ensures that the high-pass component adds complementary discriminative information without interfering with the neighborhood-preserving properties encoded in the low-frequency domain by the low-pass component. Consequently, the dual-pass embedding $\mathbf{z}_i = [\mathbf{z}_i^{\text{low}} \parallel \mathbf{z}_i^{\text{high}}]$ preserves neighborhood similarity as effectively as the low-pass component $\mathbf{z}_i^{\text{low}}$ alone, since the neighborhood-relevant information is fully retained while additional discriminative power is gained.

Claim 2 (Enhanced discriminability for node correspondence). For node correspondence tasks, the dual-pass embedding \mathbf{z}_i provides superior discriminability compared to either $\mathbf{z}_i^{\text{low}}$ or $\mathbf{z}_i^{\text{high}}$ alone. That is, false correspondences are less likely under similarity computed via \mathbf{z}_i .

Proof of Claim 2. Discriminability is measured by the separation margin between the distributions of similarities for *corresponding pairs* $\mathcal{C} = \{(i, j) : i \in \mathcal{V}_1, j \in \mathcal{V}_2, i \leftrightarrow j\}$ and *non-corresponding pairs* $\mathcal{N} = \{(i, j) : i \in \mathcal{V}_1, j \in \mathcal{V}_2, i \not\leftrightarrow j\}$.

As we mentioned, the dual-pass filter design ensures perfect spectral complementarity: the low-pass and high-pass filters have anti-correlated frequency responses, ensuring that their contributions are nearly independent. Consequently, their mutual information is bounded, $I(\mathbf{z}_i^{\text{low}}; \mathbf{z}_i^{\text{high}}) \leq \epsilon$, for small $\epsilon > 0$, reflecting the opposing spectral emphasis.

For any ℓ_2 -induced metric, the squared distance between dual-pass embeddings decomposes as:

$$d(\mathbf{z}_i, \mathbf{z}_j)^2 = d(\mathbf{z}_i^{\text{low}}, \mathbf{z}_j^{\text{low}})^2 + d(\mathbf{z}_i^{\text{high}}, \mathbf{z}_j^{\text{high}})^2 + 2\langle \mathbf{z}_i^{\text{low}} - \mathbf{z}_j^{\text{low}}, \mathbf{z}_i^{\text{high}} - \mathbf{z}_j^{\text{high}} \rangle.$$

Under the approximate orthogonality condition, the cross-term is negligible, yielding:

$$d(\mathbf{z}_i, \mathbf{z}_j)^2 \approx d(\mathbf{z}_i^{\text{low}}, \mathbf{z}_j^{\text{low}})^2 + d(\mathbf{z}_i^{\text{high}}, \mathbf{z}_j^{\text{high}})^2.$$

The separation margin is thus defined as $\Delta = \min_{(i,j) \in \mathcal{C}} \text{sim}(\mathbf{z}_i, \mathbf{z}_j) - \max_{(i,k) \in \mathcal{N}} \text{sim}(\mathbf{z}_i, \mathbf{z}_k)$.

The critical observation is that the two components offer complementary discriminative power:

- **Case A (Low-pass insufficient):** When graphs share similar global structure but differ in local details, $\mathbf{z}_i^{\text{low}}$ may yield high similarity for non-corresponding pairs. However, $\mathbf{z}_i^{\text{high}}$ captures local differences, reducing false positives.
- **Case B (High-pass insufficient):** When local structures are noisy or similar, $\mathbf{z}_i^{\text{high}}$ may be unreliable. However, $\mathbf{z}_i^{\text{low}}$ provides stable global discrimination based on community structure and smooth attributes.

Together, these effects yield an additive improvement in discriminability. Formally, the dual-pass margin satisfies

$$\Delta_{\text{dual}} \geq \max(\Delta_{\text{low}}, \Delta_{\text{high}}) + \gamma,$$

where $\gamma > 0$ represents the additional discriminative contribution from orthogonal spectral information. This establishes that the dual-pass embedding provides superior node correspondence discrimination. □

C EXPERIMENTAL SETUP

This section describes the benchmarks, performance metrics, and experimental settings used for graph alignment evaluation.

C.1 BENCHMARKS

Table 4 summarizes statistics for all experimental datasets. It includes six semi-synthetic graph alignment benchmarks consisting of graphs with varying sizes and properties to comprehensively evaluate the robustness of our approach. Additionally, two real-world graph alignment datasets with partial ground-truth node correspondences are included to assess overall performance. The datasets are as follows:

Table 4: Overview of datasets and their key properties

Dataset		#Nodes	#Edges	#Aligned Nodes	#Node Features	Description
Celegans		453	2025	453		Interactome
Arenas		1133	5451	1133		Email Communication
Douban		3906	7215	3906	7	Social Network
Cora		2708	5278	2708		Citation Network
DBLP		17716	52867	17716		Citation Network
CoauthorCs		18333	81894	18333		Coauthor
ACM-DBLP	ACM	9872	39561	6325	17	Coauthor Network
	DBLP	9916	44808			Coauthor Network
Douban	Online	3906	16328	1118	538	Social Network
	Offline	1118	3022			Social Network

- **Celegans:** This dataset models the protein-protein interaction network of *Caenorhabditis elegans*. Each node represents a protein, and edges indicate physical or functional interactions between proteins, making it useful for biological network analysis and alignment tasks involving molecular networks (Kunegis, 2013).
- **Arenas:** A communication network derived from email exchanges at the University Rovira i Virgili. Nodes correspond to individual users, and edges represent the presence of at least one email sent between them. It serves as a social interaction graph with temporal and communication patterns (Leskovec & Krevl, 2014).
- **Douban:** A social network from the Chinese movie review platform Douban, where nodes represent users, and edges capture friend or contact relationships. This dataset is commonly used to study social dynamics and network alignment in social media contexts (Zhang & Tong, 2016).
- **Cora:** A citation network of scientific papers where nodes are publications, and edges denote citation relationships. Cora is a benchmark dataset for graph mining and node classification, providing a structured academic citation graph ideal for evaluating graph-based learning models (Sen et al., 2008).
- **DBLP:** An extensive citation network aggregated from DBLP, Association for Computing Machinery (ACM), Microsoft Academic Graph (MAG), and other scholarly databases. It includes publication and citation information, widely used for testing graph alignment, clustering, and knowledge discovery tasks in academic networks (Pan et al., 2016).
- **CoauthorCs:** A co-authorship network in computer science that represents collaborations between authors. Nodes correspond to researchers, and edges indicate joint publications. It is often used to study community structure and author disambiguation in bibliographic databases (Sinha et al., 2015).
- **ACM-DBLP:** This dataset contains two co-authorship graphs from the ACM and DBLP databases. Nodes represent authors, and edges indicate co-authorship. Although collected independently, both graphs share overlapping authors, with 6,325 ground-truth alignments. Node features capture publication distributions across research venues. The dataset poses a challenging alignment task due to structural and feature discrepancies between the two graphs (Zhang & Tong, 2018).
- **Douban Online-Offline:** This dataset comprises two social graphs from the Douban platform, one based on online interactions and the other on offline event co-attendance. Both graphs share a subset of users, with 1,118 aligned nodes. Node features reflect user location distributions. The dataset is designed to evaluate alignment across heterogeneous and partially overlapping social networks (Zhang & Tong, 2016).

C.2 PERFORMANCE METRICS

To assess graph alignment performance, we adopt two widely used metrics: alignment accuracy (Acc) and Hit@ k . Alignment Accuracy (Acc) measures the proportion of correctly predicted node

correspondences among all ground-truth aligned pairs, providing a direct measure of overall matching performance. Hit@ k evaluates whether the true corresponding node from the source graph appears within the top- k predicted candidates for each node in the target graph. This metric reflects the ability of model to rank correct matches highly and is particularly useful for top- k retrieval scenarios. Both metrics are computed using all available ground-truth node pairs, with higher values indicating better alignment quality.

C.3 EXPERIMENTAL SETTINGS

In section 4.1, we follow the experimental setting introduced in the (He et al., 2024) for generating inconsistent graph pairs. Given a source graph \mathcal{G}_s with adjacency matrix \mathbf{A} , we construct 10 perturbed and permuted target graphs using the transformation $\hat{\mathbf{A}} = \mathbf{P}(\mathbf{A} + \mathbf{M})\mathbf{P}^\top$, where $\mathbf{M} \in \{-1, 0, 1\}^{N \times N}$ introduces edge-level perturbations, and \mathbf{P} is a random permutation matrix. The perturbation level is controlled by a parameter $p \in \{0, 1\%, 5\%\}$, representing the fraction of edges modified: $p|\mathcal{E}|$. We adopt seven structural node features from (Berlingerio et al., 2013): *node degree*, *clustering coefficient*, *average degree of neighbors*, *average clustering coefficient of neighbors*, *number of edges in ego-network*, *number of outgoing edges of ego-network*, and *number of neighbors of ego-network*. These descriptors provide compact, structure-aware representations for robust evaluation under varying structural inconsistencies.

As shown in Figure 2, our proposed architecture consists of two GAEs, each using a dual-pass GCN encoder with shared parameters across both modalities. The number of GCN layers is selected based on empirical performance for each benchmark: 2 layers for ACM-DBLP and the semi-synthetic datasets, 3 for DBLP, 5 for Douban, and 6 for Douban Online-Offline.

For computing functional maps, we use the first 300 eigenvectors of the graph Laplacian across all datasets. The hidden dimensions of the encoder are set to 1024 for ACM-DBLP, 256 for Douban Online-Offline, and 16 for all semi-synthetic benchmarks. For all baseline methods, we report results from the original papers when available. For cases where published results were not available on specific benchmarks (notably for GAlign and SLOAlign in Section 4.1), we re-ran the official code with default configurations to ensure a fair comparison. The model is trained end-to-end using the Adam optimizer with a learning rate of 1e-3 and a weight decay of 5e-4, based on the loss function in Equation 9.

All other hyperparameters are kept fixed across benchmarks, with values set as follows: $\alpha = 10^{-3}$, $\beta = 10^{-2}$, $\lambda_{\text{FM}} = 1$, $\lambda_{\text{bij}} = 10^{-1}$, and $\lambda_{\text{orth}} = 10^{-1}$. An ablation study on these hyperparameters is presented in Section D.

All experiments are implemented using PyTorch 2.1.2 and PyTorch Geometric 2.5.0. Most benchmarks are run on servers equipped with NVIDIA A100 GPUs (CUDA 12.2), each providing 40 GB of memory. For large-scale datasets such as DBLP and Coauthor CS, we use NVIDIA H100 GPUs (CUDA 12.6) with 95 GB of memory, enabling efficient training and evaluation on high-complexity graphs.

C.4 DETAILS OF VISION-LANGUAGE EXPERIMENT

C.4.1 SETUP

We evaluate the vision-language alignment task on a range of benchmarks, including CIFAR-10 (Krizhevsky et al., 2009), CINIC-10 (Darlow et al., 2018), CIFAR-100 (Krizhevsky et al., 2009), and ImageNet-100 (Russakovsky et al., 2015), using representations extracted from diverse pre-trained vision and language models. For each vision model, class-level representations are derived by averaging image-level embeddings within each class. Correspondingly, language representations are obtained by averaging embeddings generated from multiple textual prompts for each class. To enable application of our graph alignment method, we build a similarity graph from these representations, where each class-level embedding is treated as a node and connected to its k most similar neighbors according to cosine similarity.

Since the vision and language models generally produce embeddings of different dimensionalities, in this experiment, we employ dual-pass GCN encoders without weight sharing. While this design

accommodates modality-specific feature spaces, it also makes the alignment task more challenging, as the model must learn to reconcile heterogeneous latent representations.

C.5 HYPERPARAMETERS

We adopt a similar hyperparameter configuration for the vision-language benchmarks. Specifically, we set $k = 5$ when constructing the k -NN graphs. Each modality is encoded with a 4-layer dual-pass GCN encoder, and we use 9 Laplacian eigenvectors for CIFAR-10 and CINIC-10, and 90 eigenvectors for CIFAR-100 and ImageNet-100. The hidden and output dimensions of the encoder are both set to 512. All other hyperparameters follow the general settings described in Section C.3.

C.5.1 BASELINES

We compare against a set of established solvers and heuristics for the alignment problem. LocalCKA (Maniparambil et al., 2024) leverages the centered kernel alignment (CKA) metric to approximate the QAP with a linear assignment formulation, providing an efficient method for vision–language correspondence. Optimal Transport (OT) methods (Peyré et al., 2016) address the alignment by modeling embeddings as probability distributions and computing the minimal transport cost, thereby preserving geometric structure across modalities. The Fast Approximate QAP algorithm (FAQ) (Vogelstein et al., 2015) is a well-known primal heuristic that relaxes the QAP and iteratively refines the solution, yielding scalable but approximate alignments. MPOpt (Hutschenreiter et al., 2021) represents a generic mathematical programming approach, solving the alignment as a constrained optimization problem using standard formulations. Gurobi (Gurobi Optimization, LLC, 2023) is a commercial off-the-shelf solver for mixed-integer and quadratic programs, providing near-optimal results for small problem instances. Finally, the Hahn-Grant solver (Schnaus et al., 2025) is a dual ascent algorithm that produces strong lower bounds by repeatedly solving linear assignment problems.

We also reference two recent vision–language alignment methods. Vec2Vec (Jha et al., 2025) maps embeddings from different models into a shared latent space using input/output adapters, a shared backbone, and adversarial plus structural losses. CycleReward (Bahng et al., 2025) learns vision–language alignment via cycle-consistency-based preference data and a reward model. These models are not designed for graph alignment and therefore are not direct competitors. Moreover, a full evaluation would require reproducing their results on our benchmarks, which is beyond the scope of this work and is deferred to future studies focused specifically on this domain.

C.5.2 VISION AND LANGUAGE MODELS

We adopt the set of 32 vision models used in Blind Match (Schnaus et al., 2025). For self-supervised methods, we use DINO (Caron et al., 2021) models (RN50 and ViT-S/B with patch sizes 16 and 8) trained on ImageNet-1k and DINOv2 (Oquab et al., 2023) models (ViT-S/B/L/G with patch size 14) trained on the LVD-142M dataset, as well as fully supervised models such as DeiT variants (Touvron et al., 2021) (Tiny, Small, and Base with patch size 16, including distilled and high-resolution @384 versions) and ConvNeXt models (Liu et al., 2022b) (Base and Large, pretrained on ImageNet-1k or ImageNet-22k, with additional fine-tuned @384 variants). For vision–language pretraining, we employ CLIP (Ramesh et al., 2022) with both ResNet backbones (RN50, RN101, RN50x4, RN50x16, RN50x64) and Vision Transformer architectures (ViT-B/32, ViT-B/16, ViT-L/14, ViT-L/14@336). All experiments are conducted using official implementations and pretrained weights, ensuring consistent and reliable representation extraction for each model.

We consider four pretrained language models spanning diverse architectures and training paradigms, including the RN50x4 model from CLIP (Ramesh et al., 2022) and three models, all-MiniLM-L6-v2, all-mpnet-base-v2, and all-Roberta-large-v1, extracted from the SentenceTransformers library (Reimers & Gurevych, 2019). All vision and language models used in our experiments are summarized in Table 5.

D ABLATION ANALYSIS

To analyze the impact of individual components in the proposed framework, we conduct an ablation study evaluating variants with specific modules removed or modified. We compare GADL against:

Table 5: Summary of vision and language models used in the experiments

Vision models
DINO (Caron et al., 2021): RN50, ViT-S/16, ViT-S/8, ViT-B/16, ViT-B/8
DINOv2 (Oquab et al., 2023): ViT-S/14, ViT-B/14, ViT-L/14, ViT-G/14
DeiT (Touvron et al., 2021): DeiT-T/16, DeiT-T/16d, DeiT-S/16, DeiT-S/16d, DeiT-B/16, DeiT-B/16@384, DeiT-B/16d, DeiT-B/16d@384
ConvNeXt (Liu et al., 2022b): CN-B-1, CN-B-22, CN-L-1, CN-L-22, CN-L-22ft@384, CN-XL-22ft@384
CLIP (Ramesh et al., 2022): RN50, RN101, RN50x4, RN50x16, RN50x64, ViT-B/32, ViT-B/16, ViT-L/14, ViT-L/14@336
Language models
CLIP (Ramesh et al., 2022): RN50x4
SentenceTransformers (Reimers & Gurevych, 2019): all-MiniLM-L6-v2, all-mpnet-base-v2, all-Roberta-large-v1

(1) **GADL w/o dual-pass encoder**: replaces the dual-pass GCN with a standard single-pass GCN while retaining latent-space communication; (2) **GADL w/o bijectivity regularization**: removes the bijectivity regularization term while keeping the dual-pass encoder; (3) **GADL w/o orthogonality regularization**: omits orthogonality regularization while maintaining all other components.

Results are summarized in Table 6. They highlight the individual contribution of each component to the overall alignment performance. Replacing the dual-pass GCN with a standard encoder causes substantial accuracy drops. Furthermore, the removal of the regularization terms notably degrades performance, confirming their importance in achieving robust and reliable node alignment.

Table 6: Performance of GADL and its variants on real-world graph alignment benchmarks.

Method	ACM-DBLP				Douban Online-Offline			
	Hit@1	Hit@5	Hit@10	Hit@50	Hit@1	Hit@5	Hit@10	Hit@50
GADL w/o dual-pass encoder	81.68	92.22	95.24	97.88	43.38	62.96	71.1	88.55
GADL w/o bijectivity regularization	88.47	94.6	96.06	98.37	52.68	72.89	80.14	94.78
GADL w/o orthogonality regularization	88.51	94.48	96.06	98.35	51.96	72.8	79.51	94.72
GADL	88.63	94.76	96.16	98.41	53.31	73.61	80.67	94.18

The results also show that the dual-pass encoder provides greater improvement on Douban than ACM-DBLP, reflecting the impact of initial node features on encoder effectiveness. Essentially, the Douban dataset contains sparse, high-dimensional node features with many zero entries, causing standard GCN embeddings to become overly smooth and less discriminative. Consequently, the dual-pass filters lead to a significant improvement in matching accuracy. In contrast, the ACM-DBLP features are denser and more informative, so the standard GCN already generates sufficiently distinctive embeddings, with the high-pass component providing only moderate improvement.

E ABLATION STUDY ON GRAPH ENCODERS

We evaluate the impact of different GNN encoder architectures on the alignment accuracy within the GADL framework using two real-world benchmark datasets. Specifically, we conduct a comparative evaluation of our proposed dual-pass GCN encoder against four GNN variants: GCN (Kipf & Welling, 2017), GIN (Xu et al., 2018a), JKGNN (Xu et al., 2018b), and TIDE (Behmanesh et al., 2023). For these encoders, we adopt a 6-layer architecture with ReLU activation functions, following the configurations presented in their respective papers. Additionally, TIDE is applied in a single-channel setup, where the learnable parameter t is shared across all channels.

As shown in Figure 3, the proposed dual-pass GCN achieves consistently higher alignment accuracy across both datasets. Among the others, the GIN encoder performs best because it is designed to better capture graph structure by extending the Weisfeiler-Lehman (WL) graph isomorphism test, which helps it distinguish nodes more effectively. Since more expressive node representations reduce ambiguity in identifying correct correspondences, this enhanced expressiveness directly contributes to improved node alignment accuracy.

F HYPERPARAMETER SENSITIVITY

We conduct a sensitivity analysis to examine the influence of key hyperparameters on model performance. In particular, we focus on the loss weighting coefficients λ_{FM} , λ_{bij} , and λ_{orth} , which

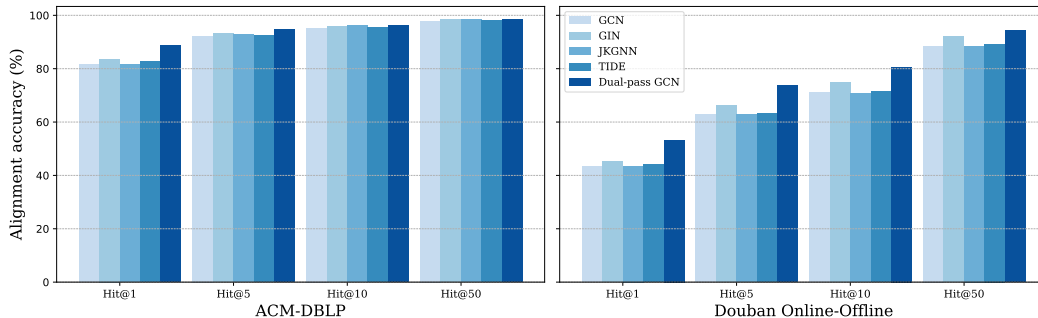


Figure 3: Encoder comparison on graph alignment performance (Hit@K).

control the relative importance of the functional map loss, bijectivity constraint, and orthogonality regularization, respectively, in the overall training objective.

To isolate the effect of each hyperparameter, we vary its value over a defined range while keeping the remaining parameters fixed at their optimal values, as determined through prior validation. We evaluate model performance using the Hit@1 accuracy metric on both real-world benchmark datasets.

The results in Figure 4 demonstrate how model performance responds to variations in each hyperparameter, using the optimal values identified through tuning as a reference. The results demonstrate that our approach is stable across a wide range of settings, while also pointing out where tuning is most important for best results. These insights provide practical guidance for selecting effective hyperparameter configurations when applying the model to new benchmarks.

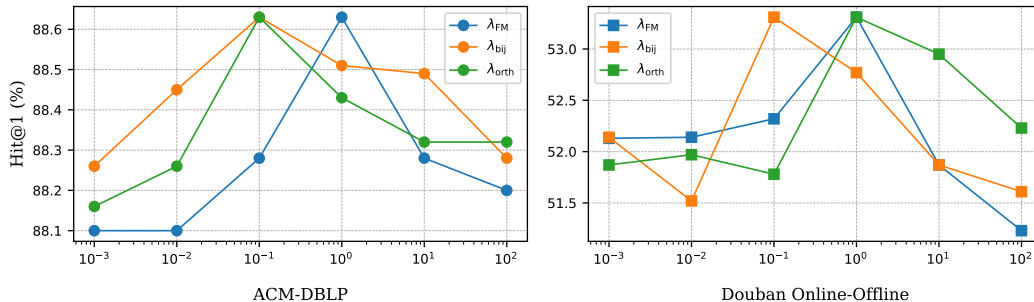


Figure 4: Hyperparameter sensitivity analysis on ACM-DBLP and Douban Online-Offline datasets. We report Hit@1 accuracy while varying each hyperparameter (λ_{FM} , λ_{bij} , λ_{orth}) independently.

G COMPREHENSIVE RESULTS FOR VISION-LANGUAGE MODEL COMBINATIONS

To provide a comprehensive evaluation of vision–language alignment, we test our proposed model across multiple vision and language model combinations on two benchmark datasets, CIFAR-10 and CINIC-10. The vision models considered include CLIP (Ramesh et al., 2022), ConvNeXt (Liu et al., 2022b), DINO (Caron et al., 2021), DINOv2 (Oquab et al., 2023), and DeiT (Touvron et al., 2021). For the language models, we include the RN50x4 model from CLIP (Ramesh et al., 2022) as well as three models from the SentenceTransformers library (Reimers & Gurevych, 2019): all-MiniLM-L6-v2, all-mpnet-base-v2, and all-Roberta-large-v1.

The results are summarized in Figure 5, where the error bars indicate the standard deviation computed over 20 random seeds.

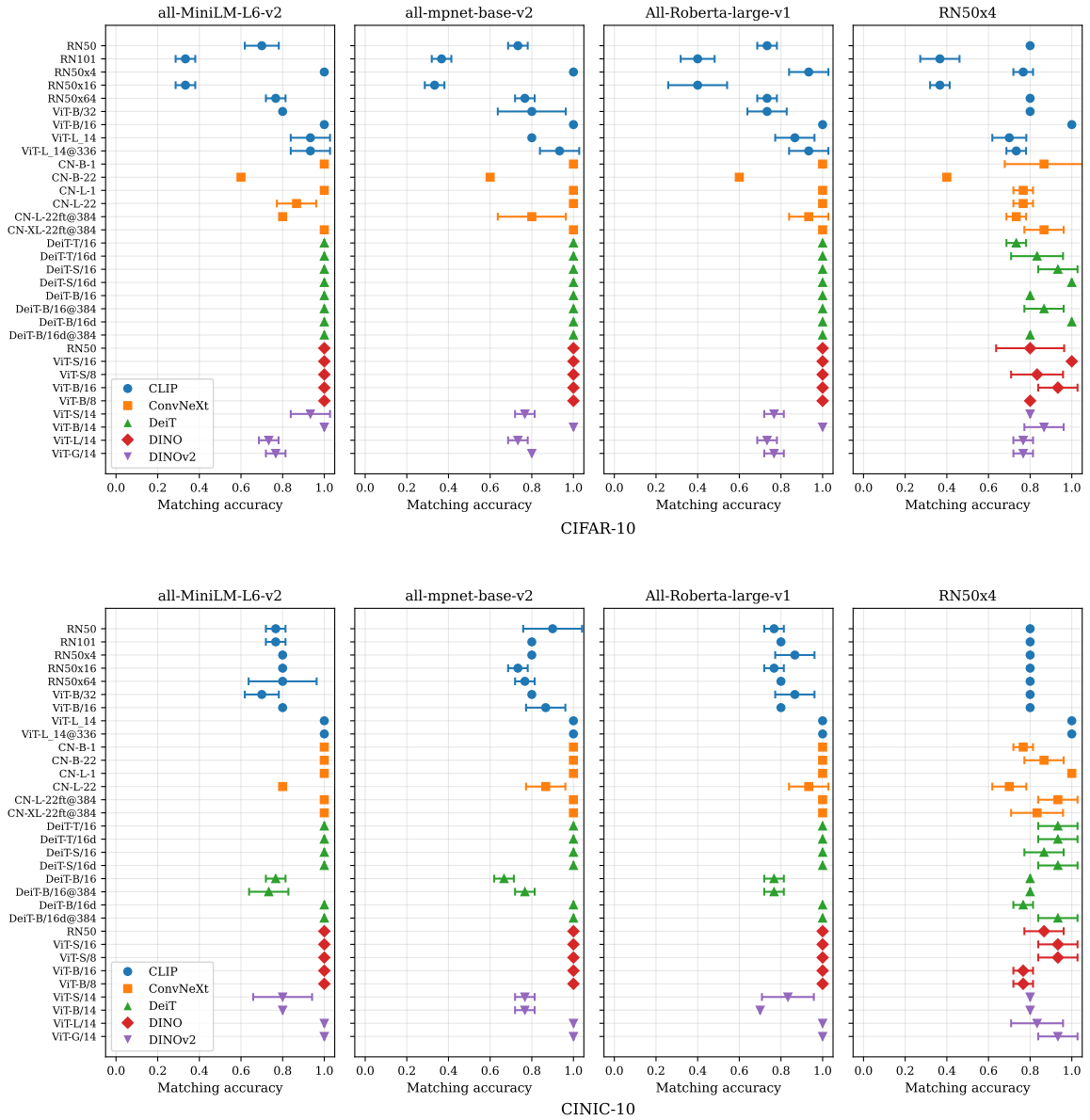


Figure 5: Vision–language accuracy of the proposed model on combinations of multiple vision models with four language models on CIFAR-10 (top row) and CINIC-10 (bottom row)

These results indicate that our proposed approach consistently achieves higher matching accuracies across diverse vision–language encoder combinations, outperforming state-of-the-art baselines such as the Hahn-Grant solver in most configurations (cf. Figure 4 in the Hahn-Grant paper (Schnaus et al., 2025)).

Our method shows particularly strong performance with DINO and DINOv2 models, where most configurations achieve matching accuracies above 0.8 on both CIFAR-10 and CINIC-10 datasets. The CLIP models also demonstrate competitive performance, with several variants reaching near-perfect accuracy. Several models achieve perfect accuracy on CIFAR-10, including CLIP: RN50x4 and ViT-B/16, all ConvNeXt variants except CN-B-22, most DeiT models, and all DINO models. Comparable trends are observed on CINIC-10, where numerous models also reach 100% accuracy. The results indicate that the choice of pre-training model has a greater influence on performance than model size. DINO models exhibit remarkable consistency, achieving near-perfect accuracy in

most configurations. In contrast, some larger models, such as CLIP: RN101 and RN50x16, perform poorly (33–40% on CIFAR-10), indicating that model scale alone does not guarantee superior performance.

Among the different language encoders, the sentence-transformer models (all-MiniLM-L6-v2, all-mpnet-base-v2, and All-Roberta-large-v1) outperform RN50x4, as they are specifically optimized for semantic text representation and generating high-quality text embeddings. In contrast, the RN50x4 encoder in CLIP is trained with an objective that prioritizes vision-language alignment rather than producing rich text embeddings.

We further evaluate the proposed model across diverse vision-language combinations on the larger-scale CIFAR-100 and ImageNet-100 benchmarks. Table 7 summarizes the results. These results demonstrate that model performance is highly context-dependent, with no single architecture achieving universal superiority across CIFAR-100 and ImageNet-100.

Table 7: Vision-language alignment accuracies on CIFAR-100 and ImageNet-100 with two language models.

Model	CIFAR-100		ImageNet-100	
	all-mpnet-base-v2	All-Roberta-large-v1	all-mpnet-base-v2	All-Roberta-large-v1
CLIP				
RN50x16	46.67 ± 2.87	67.00 ± 4.97	40.67 ± 0.94	63.67 ± 3.40
RN50x64	48.33 ± 0.47	76.33 ± 0.94	37.33 ± 0.47	58.00 ± 4.55
ViT-L/14	46.00 ± 7.87	85.67 ± 1.89	74.00 ± 0.82	61.00 ± 1.41
ViT-L/14@336	79.67 ± 2.05	81.00 ± 1.41	41.33 ± 8.26	45.33 ± 14.20
DeiT				
DeiT-B/16	47.00 ± 0.82	84.00 ± 0.82	67.33 ± 0.47	58.67 ± 4.03
DeiT-B/16@384	54.67 ± 5.44	88.00 ± 0.00	35.33 ± 0.47	57.67 ± 7.54
DeiT-B/16d	58.33 ± 8.63	58.67 ± 15.22	38.33 ± 6.02	54.33 ± 7.04
DeiT-B/16d@384	47.33 ± 8.99	42.67 ± 6.34	67.33 ± 4.50	65.67 ± 0.94
DINOv2				
ViT-B/14	48.33 ± 0.47	55.00 ± 6.53	83.67 ± 0.47	60.33 ± 0.94
ViT-S/14	48.67 ± 4.64	58.33 ± 3.22	35.67 ± 0.47	63.67 ± 4.50
ViT-L/14	79.67 ± 1.70	60.67 ± 5.19	48.33 ± 2.49	69.67 ± 7.13
ViT-G/14	67.67 ± 1.70	58.33 ± 0.47	44.33 ± 8.26	49.33 ± 0.47